

# Recent progress and prospects of integrated perovskite/organic solar cells



Cite as: Appl. Phys. Rev. **7**, 031303 (2020); doi: 10.1063/5.0013912

Submitted: 15 May 2020 · Accepted: 20 June 2020 ·

Published Online: 28 July 2020



View Online



Export Citation



CrossMark

Pang Wang,<sup>1,2</sup> Yixin Zhao,<sup>3</sup> and Tao Wang<sup>1,2,a)</sup>

## AFFILIATIONS

<sup>1</sup>School of Materials Science and Engineering, Wuhan University of Technology, Wuhan 430070, China

<sup>2</sup>State Key Laboratory of Silicate Materials for Architectures, Wuhan University of Technology, Wuhan 430070, China

<sup>3</sup>School of Environmental Science and Engineering, Shanghai Jiao Tong University, 800 Dongchuan Road, Shanghai 200240, China

<sup>a)</sup>Author to whom correspondence should be addressed: twang@whut.edu.cn

## ABSTRACT

Solar cells generate renewable energy by converting sunlight into electricity based on the photovoltaic effects. Different types of solar cells have been developed with the employment of versatile organic, inorganic, and hybrid semiconductors as the photoactive layer among which perovskite and solar cells have evidenced enormous progress in recent years. The maximum achievable power conversion efficiencies of perovskite and organic solar cells have now surpassed 25% and 18%, respectively. Nevertheless, the relatively narrow light absorption region of perovskite and large open-circuit voltage loss of organic solar cells hinder their further improvements. Recently, an emerging type of photovoltaic device, an integrated perovskite/organic solar cell, by incorporating perovskites and near-infrared organic semiconductors, has obtained enhanced short-circuit current density while reserving the high open-circuit voltage of perovskite devices. Integrated perovskite/organic solar cells simplify the sophisticated fabrication processes of tandem solar cells by depositing organic semiconductors, which are dissolved in orthogonal solvents directly onto the perovskite layer, offering a novel route to utilize more photons. In this review, we start with the operational mechanism of this new type of solar cell and then introduce various devices through distinctions of the organic layer. We proceed to summarize critical factors that determine efficiency and provide perspectives on directions to optimize, including the device structure and the organic and perovskite layers. This review serves as an ideal guide for the further development of high-performance integrated photovoltaic devices.

Published under license by AIP Publishing. <https://doi.org/10.1063/5.0013912>

## TABLE OF CONTENTS

I. INTRODUCTION .....	1
II. OPERATIONAL MECHANISM OF IPOSCS.....	2
III. THE CATEGORY OF IPOSCS .....	4
A. Binary BHJ organic materials for IPOSOSCs .....	4
B. Ternary BHJ organic materials for IPOSOSCs .....	5
C. Single-component organic materials for IPOSOSCs..	5
IV. CRITICAL FACTORS AND OPTIMIZATION	
DIRECTIONS.....	7
A. Device structure .....	7
B. Organic BHJ layer.....	7
1. Optoelectronic properties .....	7
2. Bulk heterojunction morphology.....	8
3. Recommendations of organic BHJs.....	12
C. Perovskite layer .....	13
V. CONCLUSIONS AND OUTLOOK .....	14

## I. INTRODUCTION

As one of the most direct and effective methods to utilize solar energy, solar cells have evidenced encouraging progress in the last few decades, driven by the emergence of versatile semiconductors and the design of device architectures.<sup>1–3</sup> For example, the maximum achievable power conversion efficiency (PCE) of perovskite solar cells (PSCs) has reached 25.2%, and that of organic solar cells (OSCs) has surpassed 18%.<sup>4,5</sup> Nonetheless, the maximum achievable PCEs of various single-junction solar cells are limited within the theoretical value defined by the Shockley–Queisser (S–Q) model, which is based on the principle of detailed balance equating the photon flux into a device to the particle flux (photons or electrons) out of that device.<sup>6</sup> In this S–Q framework, photovoltaic semiconductors cannot absorb the energy of photons below their bandgaps ( $E_g$ ), and photons above their bandgaps also face partial energy loss due to the thermalization of charge

carriers, resulting in ca. 45% available solar energy for photovoltaic devices. By assuming that the only charge recombination is radiative recombination, which is driven by the requirement of semiconductors to reach the thermodynamic equilibrium, the maximum achievable open-circuit voltages ( $V_{OC}$ ) are usually below their bandgaps. Taking these into account, the highest theoretical PCE of single-junction solar cells is 33.7% when the photoactive semiconductors possess an ideal bandgap of 1.34 eV.<sup>6,7</sup>

Bandgap engineering of semiconductors is a classical method to tune the photovoltaic performance of solar cells, which inevitably creates tradeoffs between photon energy loss below and above the bandgap as well as between the device metrics  $J_{SC}$  and  $V_{OC}$ .<sup>7,8</sup> How to exploit as many photons as possible is the most significant challenge to break the theoretical limit. While singlet fission can break the S–Q limit by lifting the device  $J_{SC}$ , a new challenge lies in the creation of appropriate semiconductors that can generate high yield singlet fission to practically fabricate high efficiency solar cells.<sup>9,10</sup> Combining wide and narrow bandgap semiconductors in a single device is an effective approach to fully utilize high and low energy photons simultaneously. Tandem solar cells have been developed to meet this criterion, which can directly combine perovskite, silicon, copper indium gallium diselenide, quantum dots, and organic solar cells in a multi-junction approach.<sup>11–14</sup> However, the recombination layer between the top and bottom cells complicates the fabrication process due to the requirements of energy level alignment and a high optical transmittance. Besides, the  $J_{SC}$  in series tandem solar cells and  $V_{OC}$  in parallel tandem solar cells is usually pinned to the least value of the subcell, causing undesired energy loss within devices and requiring a careful design of bandgaps and thicknesses of every subcell.<sup>15,16</sup> Therefore, tandem solar cells represent a powerful but rather complicated technology to sufficiently utilize solar photons.

Recently, emerging photovoltaic devices, called integrated perovskite/organic solar cells (IPOSs), have been introduced to acquire more photons in single devices.<sup>17,18</sup> Unlike tandem solar cells, IPOSs employ narrow-bandgap organic photovoltaic materials (usually with high  $J_{SC}$ ), which are dissolved in orthogonal solvents to directly deposit on the wide bandgap perovskite (usually with high  $V_{OC}$ ) without the presence of the recombination layer, thus simplifying the fabrication process. Benefiting from the quick development of non-fullerene narrow bandgap electron acceptors, numerous near-infrared (NIR) bulk heterojunction (BHJ) blends have been investigated in high-performance OSCs, providing new opportunities to fabricate highly efficient IPOSs via rational design and elaborate processing of the photoactive films.<sup>19–22</sup>

In this review, we start with the operational mechanism of IPOSs and then introduce different IPOSs through distinctions of the organic layer, including binary BHJ, ternary BHJ, and single-component organic materials. We proceed to summarize critical factors that determine the PCE of IPOSs and provide perspectives on directions to optimize to fabricate integrated photovoltaics with higher performance.

## II. OPERATIONAL MECHANISM OF IPOSs

The state-of-the-art OSCs usually adopt BHJ blends, consisting of electron donors (p-type semiconductor) and electron acceptors (n-type semiconductor) as the photoactive layers.<sup>22–25</sup> Charge generation of OSCs starts from photon absorption of the photoactive layer

by either donors or acceptors, with electrons promoted to the lowest unoccupied molecular orbital (LUMO) of organic semiconductors, leaving holes in the highest occupied molecular orbital (HOMO). This electron–hole pair is called exciton and has a high binding energy due to the low permittivity of organic semiconductors. Splitting of these excitons requires the diffusion of excitons to the donor/acceptor BHJ interface, where charge dissociation into free charges occurs with the LUMO level offset acting as the driving force.<sup>26</sup> Finally, the built-in field between the cathode and anode of OSCs will drive electrons to the cathode along the acceptor channel and holes to the anode along the donor channel, respectively [Fig. 1(f)].<sup>27</sup> Proper domain size and connectivity, as well as component distribution in the vertical direction of the BHJ films, have crucial influences on the dissociation of excitons and transport of charges, therefore determining the performance.

While OSCs are excitonic solar cells, PSCs are p-n junction solar cells and adopt a single-component perovskite film as the photoactive layer.<sup>1</sup> Perovskites refer to metal halide semiconductors having an  $ABX_3$  crystal structure, with A, B, X ( $A = \text{CH}_3\text{NH}_3^+$ ,  $\text{HC}(\text{NH}_2)_2^+$ ,  $\text{Cs}^+$ ;  $B = \text{Pb}^{2+}$ ,  $\text{Sn}^{2+}$ ,  $\text{Cu}^{2+}$ ,  $\text{Ge}^{2+}$ ;  $X = \text{I}^-$ ,  $\text{Br}^-$ ,  $\text{Cl}^-$ ).<sup>28</sup> The binding energy between the excited electron and hole in perovskites is substantially lower than that in organic semiconductors; therefore, free charges can be generated directly after light absorption, defining a p-n junction operational mechanism. The intrinsic ambipolar charge transport property of perovskites means that perovskites can directly generate and transport electrons and holes. Although the charge transport layer can be absent in PSCs,<sup>29</sup> high performance and stable PSCs still require the presence and dedicated design of the charge transport materials to ensure efficient charge extraction and minimize charge accumulation and recombination at interfaces [Fig. 1(g)].<sup>30–34</sup>

Typical perovskite materials, e.g.,  $\text{MAPbI}_3$  (MA = methylammonium),  $\text{MAPbI}_{3-x}\text{Cl}_x$ ,  $\text{CsPbI}_3$  (see Table IV), cannot absorb photons above 800 nm due to their wide bandgaps, resulting in high  $V_{OC}$  and limited  $J_{SC}$  of their PSC devices, and IPOSs provide the possibility to enhance the  $J_{SC}$  while maintaining the high  $V_{OC}$  via the contribution of the organic layer on top of the perovskite. The operational mechanism of IPOSs is, however, different from those of PSCs, OSCs, and typical tandem solar cells.<sup>35,36</sup> Taking inverted devices as the example, charge carrier generation and transport in IPOSs can be described as follows: (1) when devices are under illumination, the perovskite and organic materials absorb high and low energy photons, respectively, and then produce electrons and holes in both layers independently; (2) in the perovskite layer, the generated holes can be directly transferred to the anode and the electrons can transport through the continuous organic acceptor paths to cathode; (3) in the organic layer, the generated excitons are dissociated into electrons and holes at the BHJ interfaces, then electrons transport to the cathode directly and holes reach the anode through the high mobility perovskite layer. Although both perovskite and organic active layers are able to transport holes and electrons to opposite electrodes, the relatively low mobility of organic materials may induce severe recombination [Fig. 1(h)]. Due to the sufficient photo-generated charge carriers of perovskites and the low recombination velocity of organic materials, the quasi-Fermi level of IPOSs can pin in the perovskite layer, where the diffused electrons and holes from the perovskite can cause the band upward of acceptors and downward of donors to form similar quasi-Fermi level splitting to PSCs; thus, IPOSs can preserve the  $V_{OC}$  of PSC with improved  $J_{SC}$ .

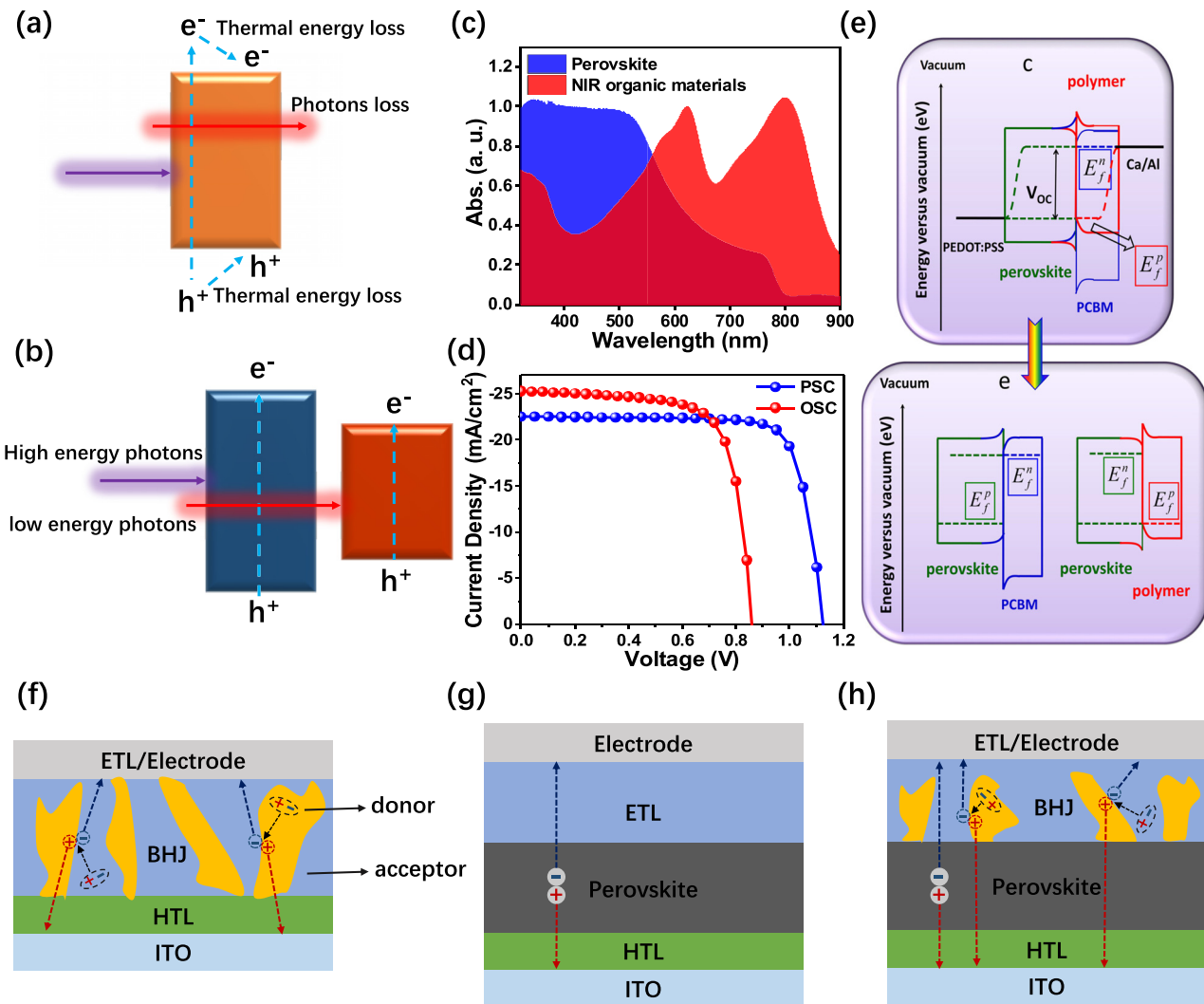


**FIG. 1.** Schematic diagram of light absorption in (a) single and (b) multi-junction solar cells. (c) Typical absorption spectra of perovskite and NIR organic materials. (d) Typical J-V curves of PSCs and OSCs. (e) Quasi-Fermi level pinning model. Reproduced with permission from Dong *et al.*, *Nano Lett.* **17**, 5140 (2017). Copyright 2017 American Chemical Society. Device structures and operation mechanisms of (f) OSCs, (g) PSCs, and (h) inverted IPOS Cs.

contributed by the NIR organic materials to enhance device performance ultimately [Fig. 1(e)].<sup>17,37,38</sup>

However, as shown in Fig. 2, J-V curves of IPOS Cs sometimes exhibit an S-shape, which indicates a poor fill factor (FF), but the corresponding origin of S-shape in IPOS Cs is also more complicated than those in OSCs and PSCs. Zhan *et al.* employed film-depth-dependent light absorption spectra to observe the light-harvesting behavior of the PTB7-Th:F8IC film on the perovskite. The blue shift of the F8IC absorption peak (800–900 nm) near the perovskite layer indicates the up-shifted LUMO level of F8IC and is associated with the decreased mobility of the BHJ layer and increased electron transport barrier between the BHJ and perovskite layers. In this condition, the electric field in IPOS Cs is strong at near zero bias and weak at near  $V_{OC}$  bias, respectively. The former could overcome the barrier caused by the up-shifted LUMO level of F8IC to facilitate electron transport from

the BHJ to perovskite, leading to a high photocurrent, whereas the latter lacks effective electron transport and causes low  $J_{SC}$  and FF. The transition point corresponds to the critical electric field for the electrons to overcome the energetic barrier.<sup>39</sup> Li *et al.* employed voltage biased EQE to investigate the contribution of photocurrent in IPOS Cs. With the increase in bias from 0 to 0.64 V, the EQE intensity above 800 nm reduced to zero gradually, but the EQE intensity below 800 nm could not reduce to zero until the bias increased to 0.82 V, demonstrating that the contribution of photocurrent was from both BHJ and perovskite layers. 0.64 and 0.82 V in voltage biased EQE correspond to the  $V_{OC}$  values of OSC and PSC, respectively, representing the different states of charge extraction at the corresponding bias in IPOS Cs, which was similar to the result of PTB7-Th:F8IC based IPOS Cs.<sup>40</sup> Therefore, the S-shape of J-V curves can be ascribed to the insufficient charge transport at different bias.

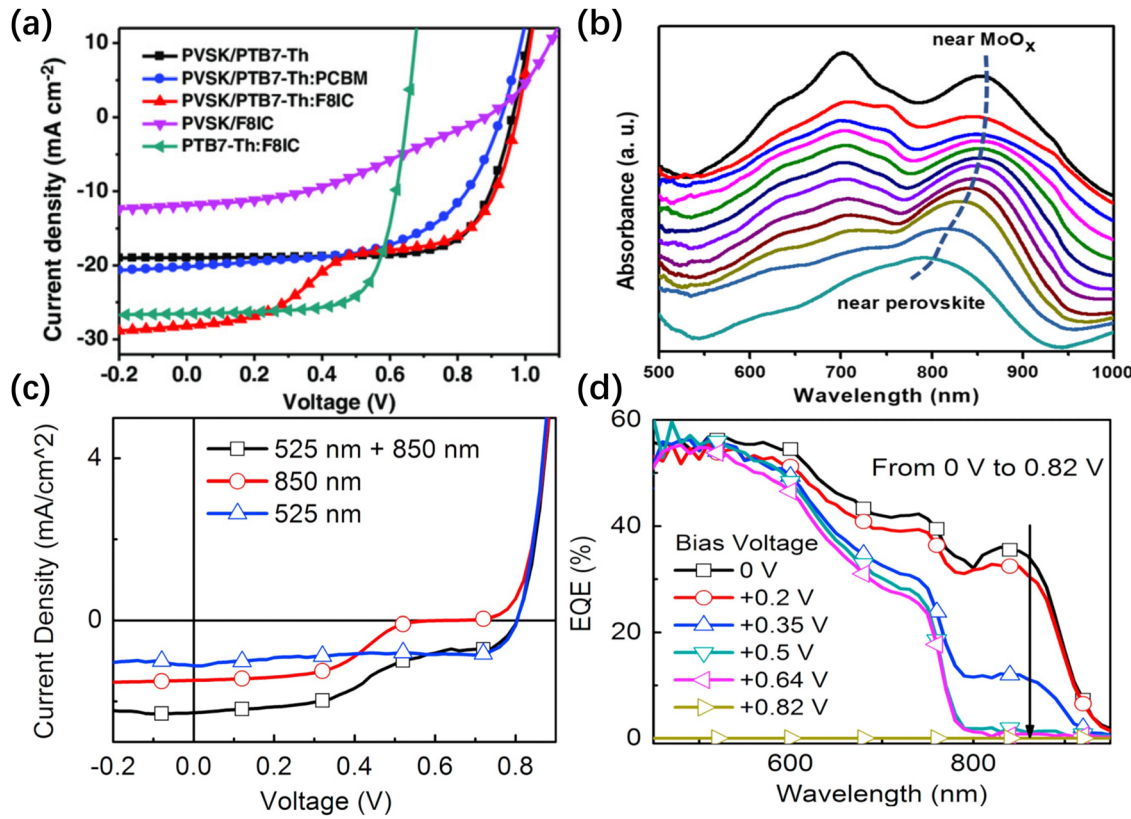


**FIG. 2.** (a) J–V curves of OSCs, PSCs, and IPOSOCs incorporating PTB7-Th, PCBM, F8IC, and their blends. The S-shaped J–V curve (e.g., the red curve) usually suggests a poor fill-factor of the device. (b) Film-depth-dependent light absorption spectra of PTB7-Th/F8IC films. The blue shift of the F8IC absorption peak (800–900 nm) indicates the up-shifted LUMO level of F8IC near the perovskite layer. Reproduced with permission from Zhang *et al.*, Sol. RRL **4**, 2000140 (2020). Copyright 2020 John Wiley and Sons, Inc. (c) J–V curves of IPOSOCs incorporating the PDPP3T/PC<sub>61</sub>BM BHJ layer under monochromatic light irradiation. (d) Voltage biased external quantum efficiency (EQE) spectra of IPOSOCs incorporating the PDPP3T/PC<sub>61</sub>BM BHJ layer. Reproduced with permission from Zhang *et al.*, Nano Energy **20**, 126 (2016). Copyright 2016 Elsevier.

### III. THE CATEGORY OF IPOSOCs

Considering the high mobility and long carrier diffusion length of perovskites, the short board of IPOSOCs to obtain high efficiency is usually the organic materials, which could introduce severe charge accumulation and recombination.<sup>41,42</sup> The selection and employment of organic materials therefore play a significant role in determining the final performance. Different types of organic materials and material combinations (see TABLE I) have been explored in recent years. We will introduce different IPOSOCs through distinctions of the organic layer, including binary BHJ, ternary BHJ, and single-component organic materials.

#### A. Binary BHJ organic materials for IPOSOCs

In 2015, Yang and co-workers employed wide- (DOR3T-TBDT) and narrow- (PBDTT-SeDPP) bandgap donors as hole transport layers in conventional (n-i-p structure) PSCs and observed low photocurrent and device performance.<sup>17</sup> However, the EQE of two devices both increased obviously after blending PC<sub>71</sub>BM with the hole transport materials [Figs. 3(a) and 3(b)]; in addition, the PBDTT-SeDPP:PC<sub>71</sub>BM based device extended its photoresponse to 900 nm

due to the NIR absorption of PBDTT-SeDPP [Figs. 3(c) and 3(d)]. They then employed rectangle pulse light to detect the photoresponse of devices upon illumination at different wavelengths. As shown in Figs. 3(e) and 3(f), there were obvious photoresponses of PBDTT-SeDPP:PC<sub>71</sub>BM based IPOSOCs upon excitation with 620 and 850 nm monochromic lights, whereas the PBDTT-SeDPP based PSCs could not provide a photoresponse under excitation at 850 nm. They concluded that the hole transport material in traditional PSCs, even with strong spectrum response capability, could not conduct to the device photocurrent unless this hole transport material formed an effective BHJ structure through blending with electron acceptors.<sup>17</sup> A similar result was reported later on by Sun *et al.* in 2016, they synthesized p-type small molecules M3 and M4 to blend with PC<sub>71</sub>BM to fabricate IPOSOCs and supported the viewpoint of Yang's work.<sup>44</sup>

Enhanced device performance of IPOSOCs have also been reported by incorporating binary BHJ organic layers without any NIR absorption characteristics.<sup>52,53</sup> Li and co-workers employed an ultrathin PBDB-T/ITIC BHJ as an interlayer to modify the interface between PEDOT:PSS and (FASnI<sub>3</sub>)<sub>0.6</sub>(MAPbI<sub>3</sub>)<sub>0.4</sub> (FA = formamidinium) perovskite.<sup>53</sup> The PBDB-T/ITIC layer was found to effectively passivate surface traps, enhance the crystallinity of perovskites, and form

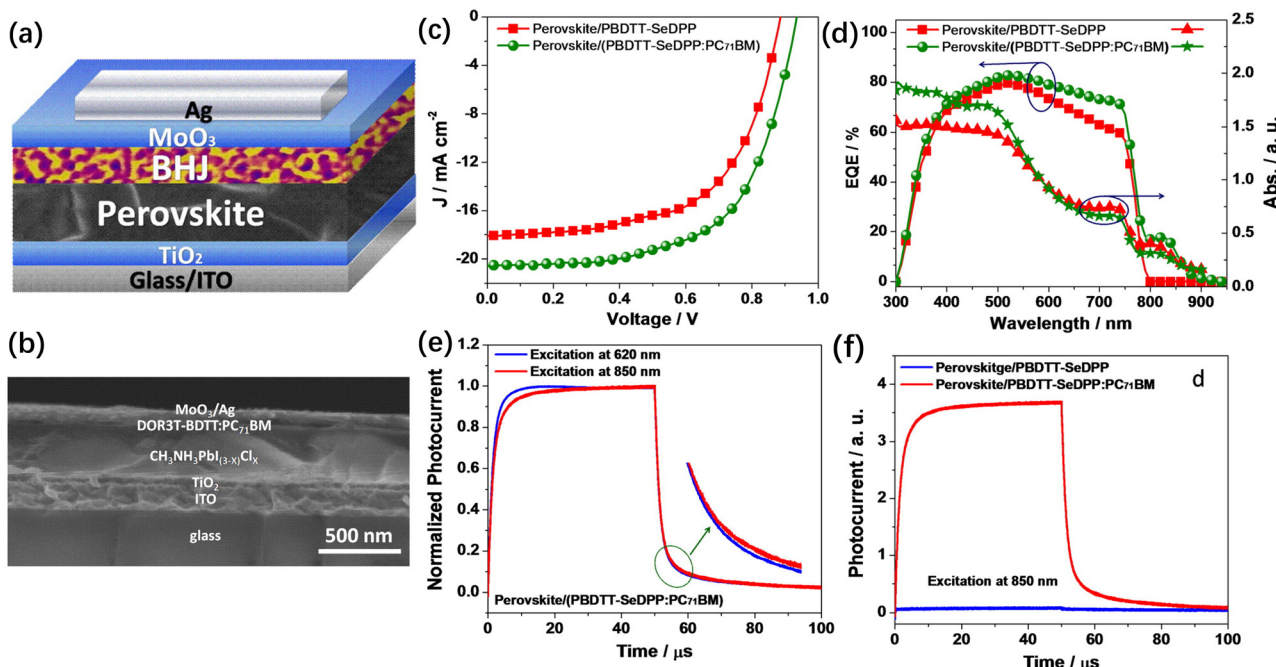


**FIG. 3.** (a) Device structure of IPOS Cs incorporating a binary BHJ organic layer. (b) Cross-sectional scanning electron microscope (SEM) image of IPOS Cs. (c) Current density–voltage ( $J$ – $V$ ) curves of PSCs and IPOS Cs. (d) EQE and absorption spectra of perovskite/hole transport layer and perovskite/BHJ based devices. Photoresponse of (e) the perovskite/BHJ device excited at 620 and 850 nm light and (f) perovskite/hole transport layer and perovskite/BHJ devices excited at 850 nm. Reproduced with permission from Liu et al., *Nano Lett.* **15**, 662 (2015). Copyright 2015 American Chemical Society.

gradient band alignment between PEDOT:PSS and perovskites, resulting in remarkable increases in  $V_{OC}$  (from 0.77 to 0.86 V) and PCE (from 15.41 to 18.03%). These works demonstrate that the BHJ interlayer can enhance the photocurrent by extending light absorption to the NIR region and by elevating crystallinity and reducing trap density of perovskites through defect passivation.

### B. Ternary BHJ organic materials for IPOS Cs

Compared to binary BHJs, ternary organic BHJs can construct more efficient OSCs because the introduction of the third component can elevate photon harvesting, promote exciton dissociation, and improve charge transport through optimization of the BHJ morphology.<sup>54</sup> Fabricating IPOS Cs through the incorporation of ternary BHJs also provides more space to enhance device performance. He and co-workers employed narrow bandgap acceptor Y6 coupled with PC<sub>61</sub>BM as a binary electron transport layer (ETL) in IPOS Cs and managed to extend the film absorption to 950 nm [Fig. 4(b)]. Although the PSCs employing the binary ETL acquired an extended photoresponse over 950 nm, the EQE intensity fell in the range from 550 to 760 nm; thus, the overall  $J_{SC}$  and PCE remained nearly unchanged [Figs. 4(c) and 4(e)]. Encouragingly, after adding the donor polymer S1 [Fig. 4(a)] to form ternary BHJs with acceptors Y6 and PC<sub>61</sub>BM, the EQE response of IPOS Cs was close to that of PC<sub>61</sub>BM based PSCs below 800 nm and reached 76% over 800 nm [see Fig. 4(f)] and fell until 950 nm, leading to a remarkable increase in  $J_{SC}$  from 22.52 to 28.06 mA/cm<sup>2</sup> [see Fig. 4(d)]. Although the PCE of this IPOS C only enhanced from 19.63 to 20.61% due to the reduced FF

from 79.1 to 67.3%, which is likely due to severe carrier recombination at the interface of ternary BHJ/perovskite,<sup>51</sup> substantially enhanced PCE can be achieved once interfacial recombination is suppressed through further dedicated investigation.

### C. Single-component organic materials for IPOS Cs

The presence of a large amount of BHJs through the phase separation of donors and acceptors is the guarantee of high efficiency exciton dissociation in OSCs.<sup>55</sup> This explains the primary reason why the first reported OSC adopting a single-component material as the active layer has an extremely low PCE, as exciton dissociation can only happen at the electrode interfaces.<sup>56</sup> Double-cable conjugated polymers can be created, which graft acceptor moieties to the conjugated backbone of donor polymers, to fabricate single-component OSCs; the difficulty to drive enough phase separation between the electron-donating and electron-accepting moieties restricts efficient exciton diffusion and charge transport, leaving a PCE below 7% at the time of writing this review.<sup>57</sup>

Although IPOS Cs incorporating double-cable organic materials have not been reported in the literature so far, a few rare cases show that single-component organic materials on top (or in the bulk) of the perovskite layer can obtain an extra photoresponse.<sup>58,59</sup> In the first work, Yang and co-workers employed a NIR narrow bandgap acceptor ITCP-M [see Fig. 5(a)] to replace PC<sub>61</sub>BM as the ETL in inverted PSCs with a structure of ITO/P3CT-Na/MAPbI<sub>3</sub>/ETL/BCP/Ag.<sup>58</sup> They employed different concentrations (from 10 to 20 mg/mL) at a constant spin speed of 2000 rpm to control the thickness of ITCP-M

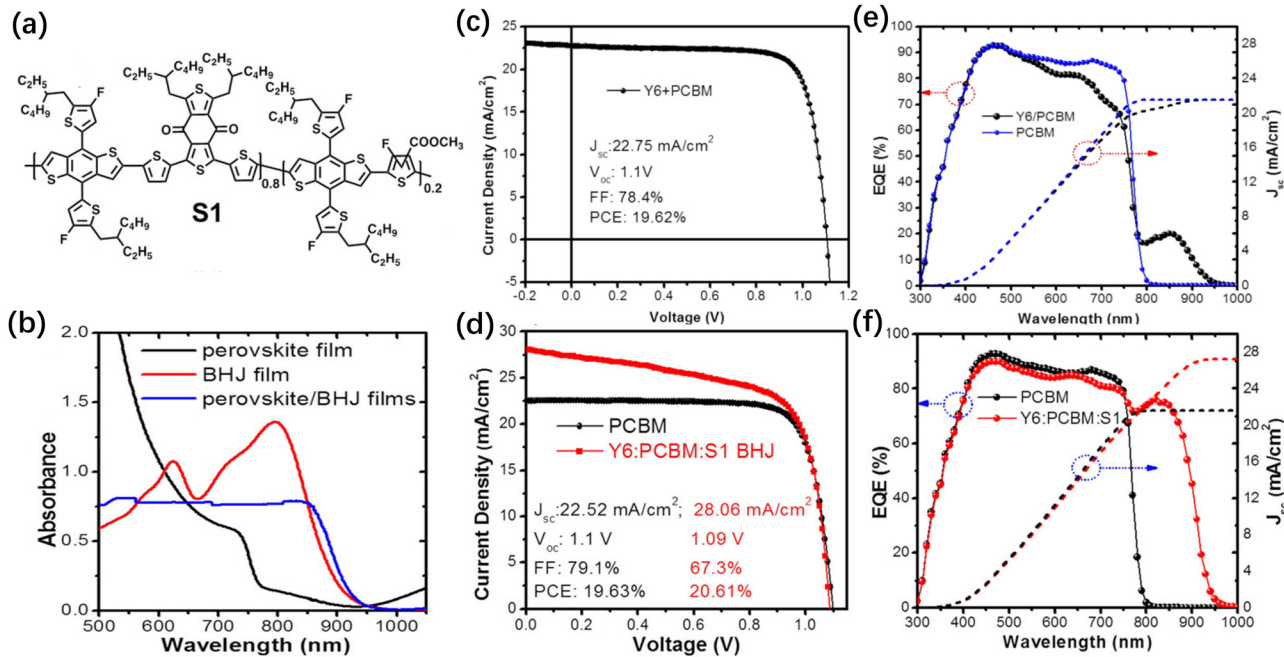


**FIG. 4.** (a) Chemical structure of S1. (b) Absorption spectra of perovskite, BHJ, and perovskite/BHJ films. (c) J–V curves and (e) EQE of PC<sub>61</sub>BM based PSCs and binary ETL based IPOS Cs. (d) J–V curves and (f) EQE of PC<sub>61</sub>BM based PSCs and ternary ETL based IPOS Cs. Reproduced with permission from Chen *et al.*, ACS Energy Lett. **4**, 2535 (2019). Copyright 2019 American Chemical Society.

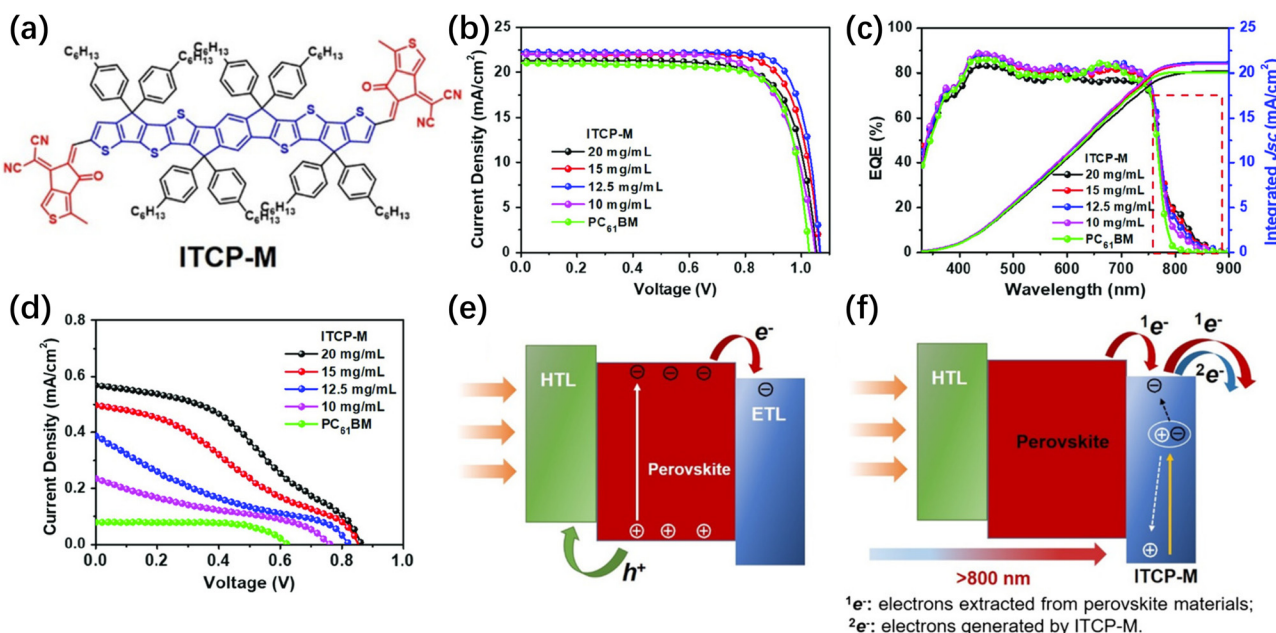


**FIG. 5.** (a) Chemical structure of ITCP-M. (b) J–V curves and (c) EQE of PC<sub>61</sub>BM and various thickness ITCP-M based devices. (d) J–V curves of devices with a light source filter of 800 nm. Possible mechanism for (e) typical PSCs and (b) ITCP-M based IPOS Cs. Reproduced with permission from Wu *et al.*, Sol. RRL **4**, 1900565 (2020). Copyright 2020 John Wiley and Sons, Inc.

in IPOS Cs, where the maximum thickness of ITCP-M approached ca. 100 nm. The ITCP-M based IPOS Cs extended their photoresponses over 800 nm, and the corresponding  $J_{SC}$  and PCE of champion devices were elevated from  $21.1 \text{ mA/cm}^2$  and 16.57% to  $22.3 \text{ mA/cm}^2$  and 18.25%, respectively, demonstrating that the single-component NIR organic material can provide the extra photocurrent in IPOS Cs [Figs. 5(b) and 5(c)]. Then they measured the J-V curves of corresponding devices under illumination with a light source filter of 800 nm and found that the current-density increased with the increasing thickness of ITCP-M [Fig. 5(d)]. Considering the thick film (ca. 100 nm) of ITCP-M and short exciton diffusion length of the organic material (ca. 10 nm),<sup>60</sup> it is the ITCP-M bulk rather than the interface of ITCP-M/perovskite that dominates the exciton dissociation process. When the ITCP-M layer is thick, the appearance of S-shaped J-V curves suggests serious charge recombination. Thus, they declared that the perovskite layer could efficiently convert photons below 800 nm to electrons and holes, and ITCP-M with an extended  $\pi$ -conjugation length could directly dissociate excitons into free electrons and holes without a donor/acceptor interface, contributing to the higher photocurrent of IPOS Cs [Figs. 5(e) and 5(f)].<sup>58</sup> Another investigation of the extended NIR photoresponse in PSCs introduced IEICO-4F into the bulk of perovskite by antisolvent rinsing, obtaining increased  $J_{SC}$  (23.6 to  $24.9 \text{ mA/cm}^2$ ) and PCE (20.4 to 21.6%).<sup>59</sup> These two works of extended NIR photoresponses in IPOS Cs (or PSCs) illustrate that the extra photoresponse can be potentially achieved by employing a single NIR organic material, but the driving force for exciton dissociation in these single-component organic materials needs to be explored further, for example, whether the adjacent perovskite and electrode layers are involved.

#### IV. CRITICAL FACTORS AND OPTIMIZATION DIRECTIONS

In order to fabricate highly efficient PSCs and OSCs, researchers have employed various approaches, including material design, dimensional tailoring, bulk morphology control, and interfacial modification, to prepare high quality films and devices.<sup>2,23,61,62</sup> While some consensuses to obtain high performance single-junction PSCs and OSCs will also apply to IPOS Cs, others have to be modified to work in IPOS Cs, and those factors applied to IPOS Cs exclusively also exist. In this section, we will illustrate the critical factors and optimization directions to obtain highly efficient IPOS Cs, including device structure, the organic BHJ layer, and the perovskite layer.

##### A. Device structure

In IPOS Cs, the BHJ layer acts as a light absorber as well as the charge transport layer; thus the donor/acceptor ratio within the BHJ layer deflects the normal value in OSCs to balance the exciton dissociation efficiency and charge transport ability.<sup>16,45</sup> In other words, the donor/acceptor ratio will reverse in inverted and conventional devices [see Figs. 6(a) and 6(b)]. In the inverted (conventional) device, the BHJ layer act as an electron (hole) transport layer and the content of the acceptor (donor) will be much more than that of the donor (acceptor). When the ratio deviates from optimum, the excess donor (acceptor) will hinder electron (hole) transport.<sup>17,37</sup> Excessive acceptors in the BHJ layer in conventional IPOS Cs in Table I may be the main origin of the low device performance.

Jen and co-workers added different amounts of PC<sub>61</sub>BM into the small molecule DPPZnP-TSEH in conventional IPOS Cs, resulting in

increased hole mobility from  $3.2 \times 10^{-5}$  to  $2.6 \times 10^{-4} \text{ cm}^2 \text{ V}^{-1} \text{ s}^{-1}$  due to the improved crystallinity of DPPZnP-TSEH and the formation of multilength scale morphology, outweighing the doped Spiro-OMeTAD [Fig. 6(c)].<sup>45,63–65</sup> With the increased ratio of PC<sub>61</sub>BM/DPPZnP-TSEH, the  $J_{SC}$  and PCE of IPOS Cs first enhanced from  $21.2 \text{ mA/cm}^2$  and 15.7% (1:10) to  $23.3 \text{ mA/cm}^2$  and 19.0% (1:4) then reduced to  $19.6 \text{ mA/cm}^2$  and 14.5% (1:1) [Fig. 6(d)], indicating the evolution of the acceptor/donor ratio from deficient to optimal and then excess values.

#### B. Organic BHJ layer

After determining the optimized device structure, how to choose organic materials and fabricate the proper BHJ layer is of the most important matter. In the development of OSCs, different narrow bandgap donors were synthesized to match the energy levels of fullerene acceptors and compensate absorption spectra. The narrow bandgap acceptors, however, were inclined to match wide bandgap donors to obtain higher performance.<sup>66,67</sup> The fullerene based OSCs with narrow bandgap donors deliver relatively low performance below 12%, much lower than the state-of-the-art non-fullerene based OSCs (featuring narrow bandgap acceptors and wide bandgap donors as the BHJ layer) with reported PCE over 18%.<sup>5,67–70</sup> Inverted IPOS Cs incorporating those narrow bandgap acceptors and wide bandgap donors as the BHJ layer have the advantage to avoid the compromise of efficient charge transport and NIR absorption in devices. Admittedly, photons below 800 nm can be well absorbed by the perovskite layer; therefore, the BHJ layer does not have to absorb high energy photons; this marks that narrow bandgap donors and acceptors can also be incorporated into IPOS Cs simultaneously if charge separation and transport are satisfactory in their BHJ OSCs. This section presents the critical factors within the organic BHJ layer and proposes some promising BHJ candidates for achieving highly efficient IPOS Cs.

##### 1. Optoelectronic properties

Organic/inorganic perovskites barely absorb photons above 800 nm and those of inorganic perovskites (e.g., CsPbI<sub>2</sub>Br) cannot absorb sunlight above 650 nm. Organic materials having a relatively high absorption coefficient to absorb photons in the NIR region can compensate light absorption of perovskites and eventually determine the upper limit of  $J_{SC}$  of IPOS Cs. This suggests that narrow bandgap NIR donors or acceptors (see examples in Fig. 7, and summarized optoelectronic properties in Table II) would be the most promising candidates to prepare the organic BHJ layer in IPOS Cs. The NIR materials should have good cascade-energy-level alignment with perovskites to guarantee small  $V_{OC}$  loss and relatively low charge recombination. For instance, the integrated perovskite/PbS quantum dot solar cells could achieve ultrahigh  $J_{SC}$  but reduced  $V_{OC}$  and FF because the bandgap of PbS quantum dots was inside that of the perovskite, leading to extensive carrier recombination.<sup>71</sup> Compared to the high mobility and excellent ambipolar charge transport property of perovskites, electron and hole mobilities of the organic BHJ layer should be as high as possible to transport charges and minimize charge accumulation and recombination. Although exciton dissociation and photoresponse can be realized in the organic layer made from single and binary acceptors, a donor/acceptor BHJ organic layer is preferred to

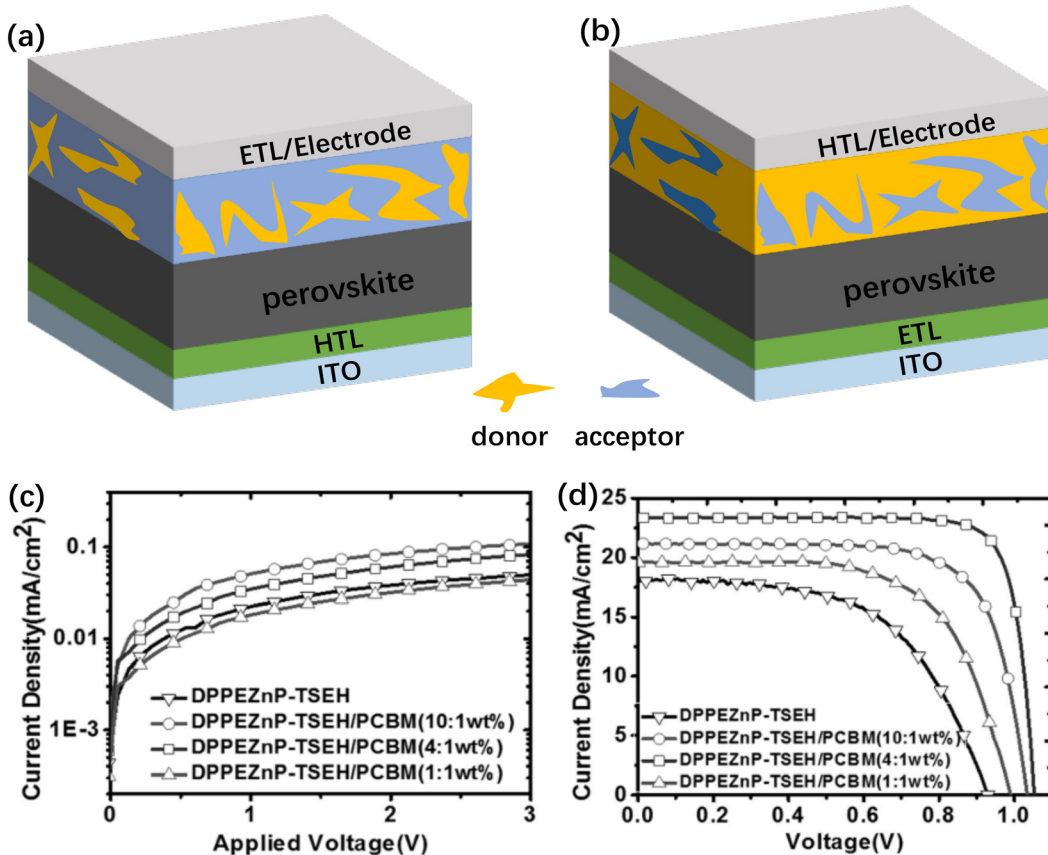


**FIG. 6.** (a) Inverted IPOS devices featuring an acceptor-rich BHJ layer and (b) conventional IPOS devices featuring a donor-rich BHJ layer. (c) Hole mobility and (d) J-V curves of IPOS devices with different DPPEZnP-TSEH/PC<sub>61</sub>BM ratios. Reproduced with permission from Gao *et al.*, *Adv. Mater.* **29**, 1703980 (2017). Copyright 2017 John Wiley and Sons, Inc.

overcome the low efficiency exciton dissociation and charge transport characteristics.<sup>48,51</sup>

## 2. Bulk heterojunction morphology

Apart from the aforementioned optoelectronic properties of NIR organic materials, efforts have to be dedicated to the fabrication process of the organic BHJ layer to develop desired morphology to ensure efficient exciton dissociation and high mobility charge transport in IPOS devices.<sup>45,46,48</sup> The desired nanoscale morphology of the BHJ layer prefers bi-continuous connectivity of donors and acceptors, with the phase separated domain size not more than 20 nm as the exciton diffusion length in organic semiconductors is usually less than 10 nm.<sup>35,60,78,79</sup> This guarantees that excitons can reach the donor/acceptor interface to dissociate rather than decay. Charge mobility will be enhanced with improved structural order; therefore, high crystallinity of the organic semiconductor will be beneficial, providing that the high crystallinity will not induce excessive phase separation between donors and acceptors.<sup>80</sup> The fibril network is a promising morphology for the BHJ layer, as the ordered molecule packing promotes high mobility charge transport along the fibril, and nanoscale fibrils formed by both polymer donors and non-fullerene acceptors have been

reported in the literature.<sup>81,82</sup> The nanoscale morphology of the BHJ layer can be controlled through aggregation in the solution state,<sup>83</sup> during solution casting (e.g., additive modification,<sup>84,85</sup> hot substrate casting,<sup>23</sup> and solvent vapor atmosphere casting<sup>55</sup>) and upon post-treatment of solid state films (e.g., thermal annealing<sup>86</sup> and solvent annealing<sup>65,87</sup>). A number of review papers can be referred for obtaining further details on morphology control of OSCs to reach high performance.

Lee and co-workers reported the influence of BHJ morphology of the organic layer on the performance of IPOS devices. They first employed the TT/PC<sub>71</sub>BM BHJ layer to replace PC<sub>61</sub>BM as an ETL in IPOS devices, obtaining a relatively low PCE of 14.85%. After adding a proper amount of diphenyl ether (DPE) and polymeric acceptor N2200 successively, device performances were elevated to 15.72 and 16.36%, respectively, much higher than those of the PC<sub>61</sub>BM based PSCs (14.7%) [Fig. 8(d)]. Atomic force microscope (AFM) and transmission electron microscope (TEM) images of the TT/PC<sub>71</sub>BM BHJ layers showed large phase separation of the blend, and the introduction of DPE and N2200 into the chlorobenzene (CB) solvent promoted the appropriate phase separation and induced pronounced fibril networks, which were beneficial for exciton dissociation and charge transport [Figs. 8(a) and 8(b)]. As a result, the electron mobility increased from

**TABLE I.** Binary and ternary BHJs incorporated into IPOS Cs.

Device structure	D:A or D:A <sub>1</sub> :A <sub>2</sub> ratio	BHJ thickness (nm)	Elevated J <sub>SC</sub> (mA/cm <sup>2</sup> )	Elevated PCE (%)	Refs.
Inverted structure with binary BHJ					
ITO/PEDOT:PSS/MAPbI <sub>3-x</sub> Cl <sub>x</sub> /PDPP3T:PC <sub>61</sub> BM	1:4	80	13.1–13.9	9.5–8.8	<a href="#">37</a>
ITO/PEDOT:PSS/MAPbI <sub>3-x</sub> Cl <sub>x</sub> /PDPP3T:PC <sub>61</sub> BM	1:4	90	18.2–22.9	10.2–12.2	<a href="#">43</a>
FTO/PEDOT:PSS/MAPbI <sub>3</sub> /PDPP3T:PC <sub>61</sub> BM	1:2	100	14.8–14.8	8.9–9.3	<a href="#">40</a>
ITO/PEDOT:PSS/MAPbI <sub>3-x</sub> Cl <sub>x</sub> /PDTP-DFBT: PC <sub>71</sub> BM	1:2	65	19.6–21.1	14.2–15.8	<a href="#">38</a>
Conventional structure with binary BHJ					
ITO/TiO <sub>2</sub> /MAPbI <sub>3-x</sub> Cl <sub>x</sub> /PBDTT-SeDPP:PC <sub>71</sub> BM	1:2	70	18.1–20.6	9.7–12.0	<a href="#">17</a>
FTO/TiO <sub>2</sub> /(FAPbI <sub>3</sub> ) <sub>0.85</sub> (MAPbBr <sub>3</sub> ) <sub>0.15</sub> /M4:PC <sub>71</sub> BM	1:1.3	110	19.7–24.0	13.2–15.0	<a href="#">44</a>
ITO/SnO <sub>2</sub> /C <sub>60</sub> /MAPbI <sub>3</sub> /DPPZnP-TSEH:PC <sub>61</sub> BM	4:1	110	21.4–23.3	17.1–18.3	<a href="#">45</a>
FTO/TiO <sub>2</sub> /MAPbI <sub>3</sub> /PBDTTT-E-T:IEICO	1:1.25	130	21.8–24.5	18.1–14.6	<a href="#">46</a>
ITO/SnO <sub>2</sub> /CsPbI <sub>2</sub> Br/PBDTTT-E-T:IEICO	1:1.25	90	14.8–16.0	12.5–14.0	<a href="#">47</a>
FTO/TiO <sub>2</sub> /MAPbI <sub>3</sub> /PBDB-T:IEICO	1:0.7	110	21.8–23.1	12.6–15.5	<a href="#">16</a>
ITO/SnO <sub>2</sub> /C <sub>60</sub> /MAPbI <sub>3-x</sub> Cl <sub>x</sub> /PTB7-Th:F8IC	1:1.5	...	19.0–28.2	13.3–12.8	<a href="#">39</a>
Ternary BHJ					
ITO/NiO <sub>x</sub> /(FAPbI <sub>3</sub> ) <sub>0.85</sub> (MAPbBr <sub>3</sub> ) <sub>0.15</sub> /PBDB-TF: BT-CIC:PC <sub>61</sub> BM	1:1.3	...	20.7–22.5	18.9–18.0	<a href="#">48</a>
ITO/PEDOT:PSS/VO <sub>x</sub> /MAPb(I <sub>1-x</sub> Br <sub>x</sub> ) <sub>3</sub> /TT: PC <sub>71</sub> BM:N2200	1:3:0.25	100	17.6–20.3	14.7–16.4	<a href="#">49</a>
ITO/PTAA/PFN/MAPbI <sub>3</sub> /TT: PC <sub>71</sub> BM:N2200	1:5:0.25	200	19.9–22.1	17.5–17.7	<a href="#">50</a>
ITO/PTAA/CsFAMAIBr/S1:PC <sub>61</sub> BM:Y6	0.5:1:1	...	22.5–28	19.6–20.6	<a href="#">51</a>

$9.6 \times 10^{-4}$  (of TT/PC<sub>71</sub>BM) to  $7.8 \times 10^{-3}$  (of TT/PC<sub>71</sub>BM:DPE) and  $1.2 \times 10^{-2}$  (of TT/PC<sub>71</sub>BM/N2200:DPE) cm<sup>2</sup> V<sup>-1</sup> s<sup>-1</sup>, and the corresponding hole/electron mobility became more balanced (from 11.6 to 0.30 and 0.32, respectively), which were conducive to enhance device performance [Fig. 8(c)].<sup>49</sup>

Out-of-plane morphology of the photoactive layer, i.e., vertical stratification or vertical component distribution, can significantly influence charge transport and injection toward electrodes and therefore impacts the performance of OSCs.<sup>90,91</sup> A rich amount of donors near the anode interface or acceptors near the cathode interface can favor charge carrier injection into electrodes, therefore minimize charge accumulation and recombination in the organic BHJ layer. This helps to minimize V<sub>OC</sub>, J<sub>SC</sub>, and FF losses in IPOS Cs. Vertical stratification can be tuned via the donor/acceptor ratios, material property as well as film casting conditions.<sup>90</sup> For example, Cho *et al.* synthesized P3HT derivatives with different end groups to match the surface energy of PC<sub>61</sub>BM. Compared to larger surface energy of P3HT-Br, P3HT-OH, and P3HT-CH<sub>3</sub>, P3HT-CF<sub>3</sub> possessing similar surface energy with PC<sub>61</sub>BM could induce less vertical phase separation with a smaller PC<sub>61</sub>BM domain size in BHJ film, resulting in better device performance before and after thermal annealing.<sup>92</sup> Jen *et al.* employed an off-center method to construct effective vertical component distribution of PTB7-Th:PC<sub>71</sub>BM. The traditional spin-coating method induced a steep donor/acceptor composition gradient in vertical direction, whereas the off-center method could form a more favorable vertical composition gradient in the BHJ film, overcoming the dramatic decrease in FF in thick films and acquiring PCE of OSCs approaching 11%.<sup>93</sup> Tan and co-workers fabricated

PBDB-T:IEICO based IPOS Cs with a structure of FTO/TiO<sub>2</sub>/MAPbI<sub>3</sub>/PBDB-T:IEICO/MoO<sub>3</sub>/Ag. They optimized the donor/acceptor weight ratio to construct the bi-continuous interpenetrating network and tailor the vertical stratification within the PBDB-T:IEICO layer. As shown in Figs. 9(a) and 9(b), when the donor/acceptor ratio was 1:1 and 1:0.7, IEICO and PBDB-T enriched at the BHJ/electrode interface, respectively, and the three-dimensional cartoons of vertical component distribution clearly manifested this tendency. The rich PBDB-T near anode ensured smooth charge transport and effectively inhibited charge recombination, and thus elevated the PCE from 12.63 to 15.47% in these IPOS Cs.<sup>16</sup>

Ideally, lateral and vertical morphologies of the BHJ layer need to be optimized simultaneously to achieve the best performance of IPOS Cs. Chueh and co-workers blended PC<sub>61</sub>BM and non-fullerene NIR acceptor BT-CIC as a binary ETL in IPOS Cs.<sup>48</sup> According to the internal quantum efficiency (IQE) and EQE spectra, the binary acceptor blends could extend absorption to the NIR region and generate excitons but failed to effectively increase the NIR photoresponse of IPOS Cs due to the poor hole-transporting property of the binary acceptor layer. After adding the polymer donor into the binary ETL, hole and electron mobility were significantly enhanced and the photo-response was extended over 900 nm, leading to an improved J<sub>SC</sub> from 17.6 (binary ETL blends) to 20.0 (ternary BHJ blends with PBDB-T as the donor) and 20.3 mA/cm<sup>2</sup> (ternary BHJ blends with PM6 as the donor). The better performance of PM6:BT-CIC:PC<sub>61</sub>BM ternary BHJ blend based IPOS Cs is attributed to the deeper HOMO energy level and better charge transport capability of PM6 compared to PBDB-T, which are beneficial to charge transport and extraction at the interface

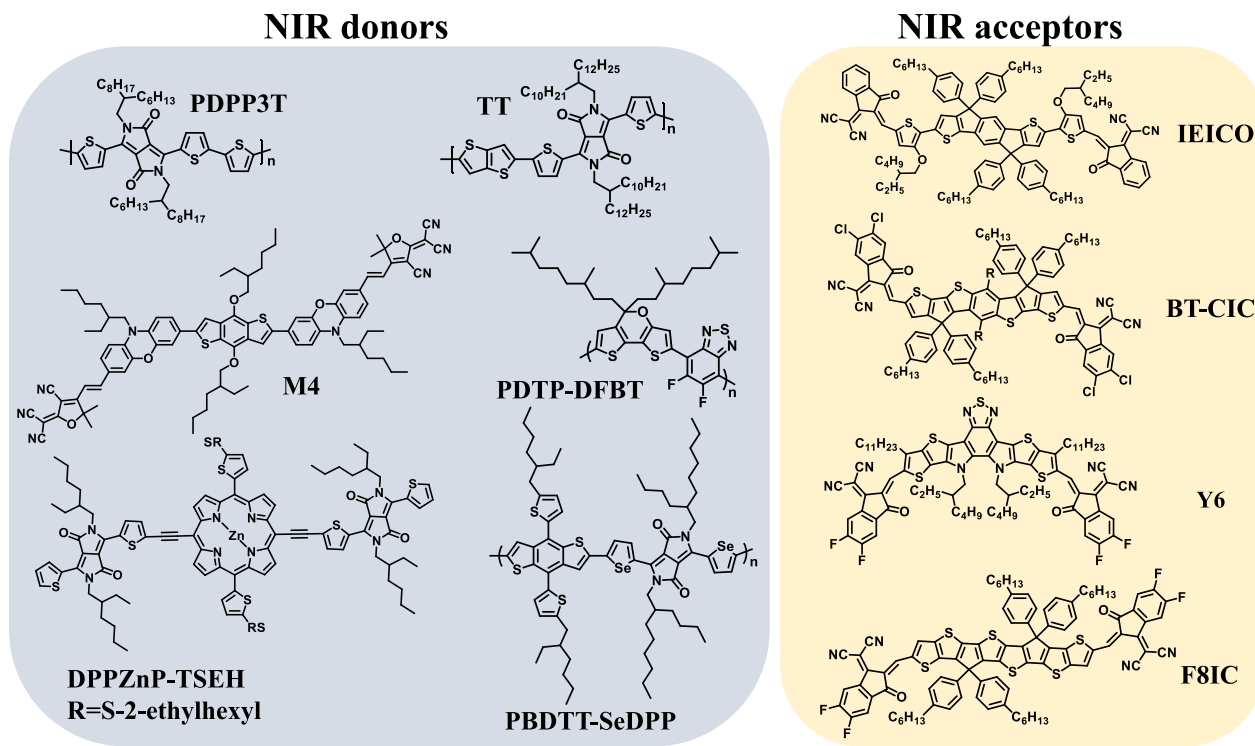


FIG. 7. Chemical structures of some NIR donors and acceptors investigated in IPOSAs.

of ternary BHJ blends/perovskite. Then they employed additives to tailor the lateral and vertical morphology in the BHJ layer. Compared to the pristine film (PM6:BT-CIC:PC<sub>61</sub>BM), the ternary BHJ blends with the addition of DPE showed a more conspicuous fibril network, and

the BHJ layer with a PM6:BT-CIC ratio ≈ 1 was extended deeper in the vertical direction [Figs. 9(c) and 9(d)]. The better lateral morphology and vertical stratification of the ternary BHJ layer were beneficial to charge transport and extraction, leading to a final PCE of 18.0%.<sup>48</sup>

TABLE II. Optoelectronic properties of NIR donors and acceptors investigated in IPOSAs.

NIR materials	HOMO (eV)	LUMO (eV)	Electrochemical Eg (eV)	Optical Eg (eV)	Hole or electron mobility ( $\times 10^{-4}$ cm <sup>2</sup> V <sup>-1</sup> s <sup>-1</sup> )	Refs.
<b>Donors</b>						
PDPP3T	-5.17	-3.61	1.56	1.30	4 <sup>a</sup>	72
TT	-5.10	-3.68	1.42	1.35	15000 <sup>a</sup>	73
PDTP-DFBT	-5.26	-3.64	1.62	1.38	30 <sup>b</sup>	74
PBDTT-SeDPP	-5.30	-3.70	1.60	1.38	...	75
M4	-5.18	-3.74	...	1.44	1.29 <sup>b</sup>	44
DPPZnP-TSEH	-5.20	-3.82	...	1.38	0.32 <sup>b</sup>	45
<b>Acceptors</b>						
F8IC	-5.43	-4.00	1.43	1.27	15 <sup>b</sup>	76
BT-CIC	-5.49	-4.09	1.40	1.33	...	77
IEICO	-5.32	-3.95	1.37	1.34	1.4 <sup>b</sup>	25
Y6	-5.65	-4.10	1.55	1.33	2.35 <sup>b</sup>	22

<sup>a</sup>Mobilities of organic materials are measured by field-effect transistor methods.<sup>b</sup>Mobilities of organic materials are measured by space charge limited current.

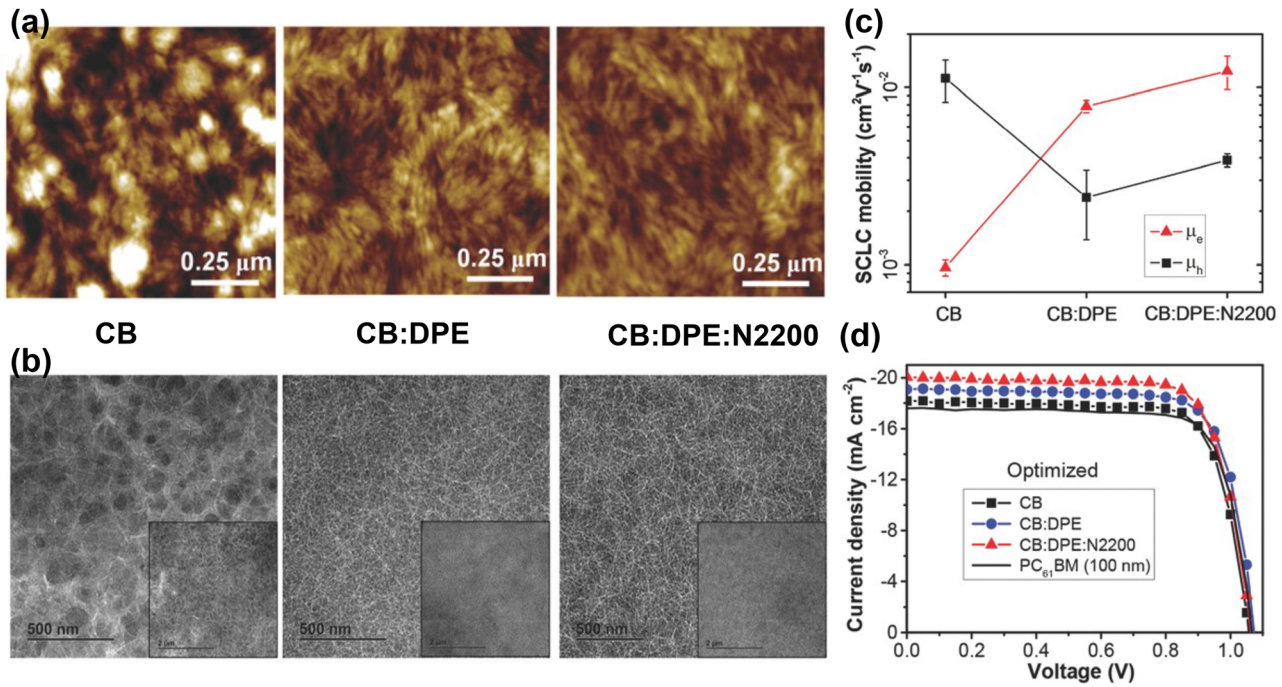


**FIG. 8.** (a) AFM, (b) TEM images, and (c) electron and hole mobilities of CB, CB:DPE, and CB:DPE:N2200 processed BHJ films. (d) J-V curves of PC<sub>61</sub>BM- and BHJ film-based devices. Reproduced with permission from Kim *et al.*, *Adv. Mater.* **28**, 3159 (2016). Copyright 2016 John Wiley and Sons, Inc.

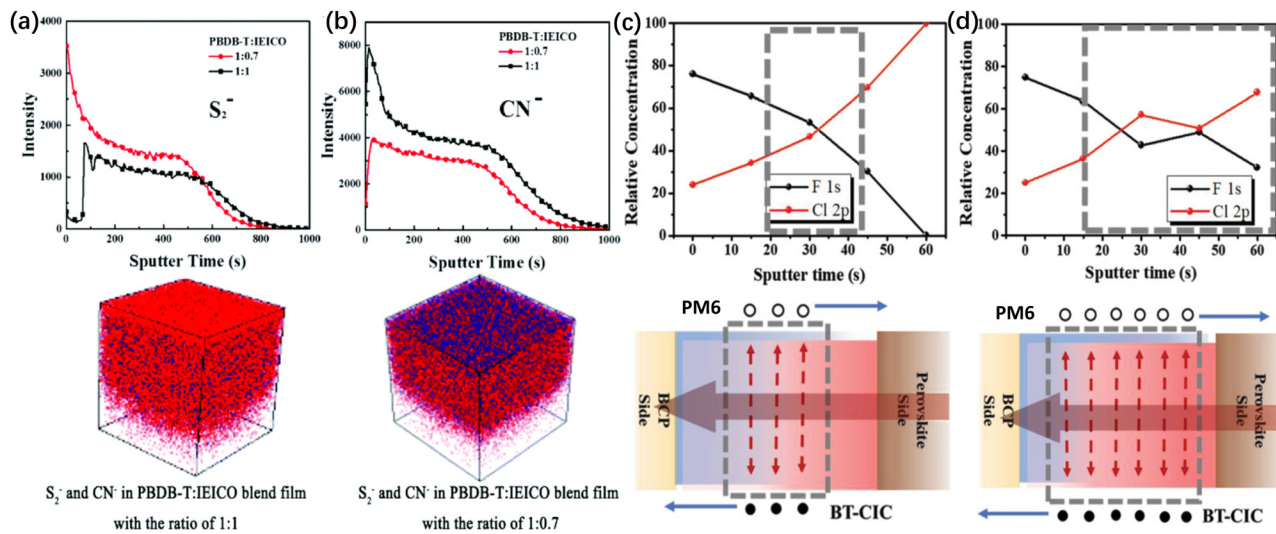


**FIG. 9.** Time-of-flight secondary-ion mass spectroscopy depth profile of (a) S<sub>2</sub><sup>-</sup> (representing PBDB-T) and (b) CN<sup>-</sup> (representing IEICO) signals in PBDB-T:IEICO BHJ having two different ratios, with sputter time of 0 corresponding to the BHJ surface. The bottom shows respective three-dimensional cartoons of vertical stratification in the PBDB-T:IEICO BHJ layer. Reproduced with permission from Wang *et al.*, *Nanoscale* **11**, 4035 (2019). Copyright 2019 Royal Society of Chemistry. XPS element intensity of F (representing PM6) and Cl (representing BT-CIC) atoms and associated illustration for vertical stratification in (c) ternary BHJ and (d) ternary BHJ processed with 1 wt. % DPE. Reproduced with permission from Chen *et al.*, *Adv. Sci.* **6**, 1901714 (2019). Copyright Authors, licensed under a Creative Commons Attribution 3.0.

### 3. Recommendations of organic BHJs

With the continuous development and emergence of new organic semiconductors for OSCs, the choice of BHJ organic materials for IPOSOS becomes versatile, and we proceed to recommend a few promising candidates to achieve high efficiency. BHJ based OSCs with an EQE spectrum onset over 900 nm featuring NIR absorption and photoresponse, high charge mobility, and a PCE higher than 12% are the primary selection criterion, although the recommendations below and the list in [Table III](#) are never exclusive.

*a. Thickness-insensitive OSCs.* Most organic semiconductors possess a charge mobility in the range of  $10^{-3}$  to  $10^{-5} \text{ cm}^2 \text{ V}^{-1} \text{ s}^{-1}$  and exhibit serious thickness-dependence, when mobility reduces dramatically with increasing film thickness. This will result in a trade-off between sufficient light absorption (which enhances with increasing film thickness) and efficient charge transport (which reduces with increasing film thickness). For example, Ding *et al.* reported the PDPP3T/PC<sub>61</sub>BM BHJ layer on top of perovskites to fabricate inverted IPOSOS, with the thickness of the BHJ layer ranging from 45 to 130 nm. The thin BHJ film (45 nm) generated insufficient NIR photocurrent, whereas an excess BHJ film thickness (130 nm) decreased the photoresponse between 500 and 800 nm. The optimal BHJ film around 80 nm could balance the generation and transport of charge

carriers to obtain the highest  $J_{SC}$  [[Figs. 10\(a\)](#) and [10\(b\)](#)].<sup>37</sup> The optimal thickness of the BHJ layer in IPOSOS varies according to literature reports summarized in [Table I](#). A number of organic semiconductors have been reported to exhibit thickness insensitivity, e.g., IDT-OB, SeTIC4Cl, PFBT4T-C5Si, and their resultant OSCs delivered decent PCE across a broad thickness range.<sup>94–96</sup> Adopting thickness insensitive organic BHJ layers in the IPOSOS is beneficial to fabricate thick BHJ films to absorb as many photons as possible in the NIR region at a minor cost of charge transport ability. [Table III](#) summarizes some thickness-insensitive organic BHJs with the absorption onset longer than 800 nm for IPOSOS applications. Taking the PM6:SeTIC4Cl BHJ film for example, the PCEs of the resultant OSCs are not strongly dependent on the thickness of the BHJ layer due to their high mobility ( $\sim 10^{-3} \text{ cm}^2 \text{ V}^{-1} \text{ s}^{-1}$ ), which can hold 85% of maximum PCE with the thickness ranging from 50 to 300 nm [[Figs. 10\(c\)](#) and [10\(d\)](#)].<sup>19,94</sup>

*b. Y6 derivative based OSCs.* The non-fullerene electron acceptor Y6 emerged as the star material in the last couple of years, featuring an EQE onset in the NIR region around 950 nm and decent mobility of  $2.35 \times 10^{-4} \text{ cm}^2 \text{ V}^{-1} \text{ s}^{-1}$ .<sup>5,22</sup> Alkyl chain engineering and terminal unit engineering in Y6 derivatives generate more promising NIR acceptors, e.g., N3, BTP-4Cl, and BTP-eC9, to tune molecular packing and morphology of corresponding BHJ films, resulting in encouraging

**TABLE III.** Promising BHJ layers for high-performance IPOSOSs.

BHJ	EQE onset (nm)	Mobility ( $\text{cm}^2 \text{ V}^{-1} \text{ s}^{-1}$ )		$J_{SC}$ ( $\text{mA}/\text{cm}^2$ )	PCE (%)	PCE range (%)		Refs.
		Hole	Electron			[thickness (nm)]		
Thickness insensitive series								
PM6:SeTIC4Cl	900	$1.6 \times 10^{-3}$	$3.0 \times 10^{-3}$	22.9	13.3	11.3–13.3 (50–300)		19
PM6:IT-4F:O6T-4F	950	$7.3 \times 10^{-4}$	$2.6 \times 10^{-4}$	21.6	13.4	12.0–13.4 (100–300)		99
PBDB-T:IDT-OB	780	$2.1 \times 10^{-4}$	$2.7 \times 10^{-4}$	16.2	10.1	8.5–10.1 (50–300)		94
PBDB-T-SF:IDIC:ID4F	800	$2.2 \times 10^{-4}$	$2.9 \times 10^{-4}$	16.9	11.5	10.1–11.5 (85–250)		95
PFBT4T-C5Si:PC <sub>71</sub> BM	800	$9.7 \times 10^{-3}$	$5.1 \times 10^{-3}$	19.1	11.1	9.1–11.1 (150–600)		96
Y6 series								
PM6:Y6	950	$2.0 \times 10^{-4}$	$5.9 \times 10^{-4}$	25.3	15.7	13.6–15.7 (150–300)		22
D18:Y6	950	$1.5 \times 10^{-4}$	$1.4 \times 10^{-4}$	27.7	18.2	18.2 (103)		5
PM6:BTP-4Cl	950	$2.1 \times 10^{-4}$	$1.6 \times 10^{-4}$	25.4	16.5	12.9–16.5 (70–300)		100
PM6:BTP-eC9	950	...	...	26.2	17.8	17.8 (100)		69
PM6:Y6:BTP-M	950	$3.4 \times 10^{-3}$	$1.4 \times 10^{-3}$	26.6	17.0	13.5–17.0 (120–400)		101
PM6:Y6:PC <sub>71</sub> BM	950	...	...	25.7	16.7	...		97
PM6:Y6:IDMIC-4F	950	$6.9 \times 10^{-4}$	$7.5 \times 10^{-4}$	25.3	16.6	16.6 (130)		82
PM6:N3:PC <sub>71</sub> BM	950	...	...	25.7	16.7	16.7 (105)		102
PTQ10:Y6:PC <sub>71</sub> BM	950	$1.9 \times 10^{-4}$	$3.3 \times 10^{-4}$	25.3	16.1	16.1 (100–110)		98
Other BHJs								
PTB7-Th:IEICO-4F	1000	$1.4 \times 10^{-4}$	$1.5 \times 10^{-4}$	27.3	12.8	9.3–12.8 (52–257)		103
Si25-H2:IEICO-4F	1000	$4.1 \times 10^{-3}$	$9.2 \times 10^{-4}$	26.9	13.2	10.3–13.2 (150–460)		104
PTBSi25:IEICO-4F	1000	$3.6 \times 10^{-4}$	$1.7 \times 10^{-4}$	25.6	12.6	...		105
PTB7-Th:CO <i>i</i> 8DFIC	1050	$5.1 \times 10^{-4}$	$2.4 \times 10^{-4}$	27.3	13.8	13.8 (100)		23
PM6:DTTC-4Cl	950	$6.2 \times 10^{-4}$	$7.9 \times 10^{-4}$	21.5	15.4	...		106
PM6:IT-4F:F8IC	1000	$4.3 \times 10^{-3}$	$4.4 \times 10^{-3}$	25.6	14.2	14.2 (115)		107

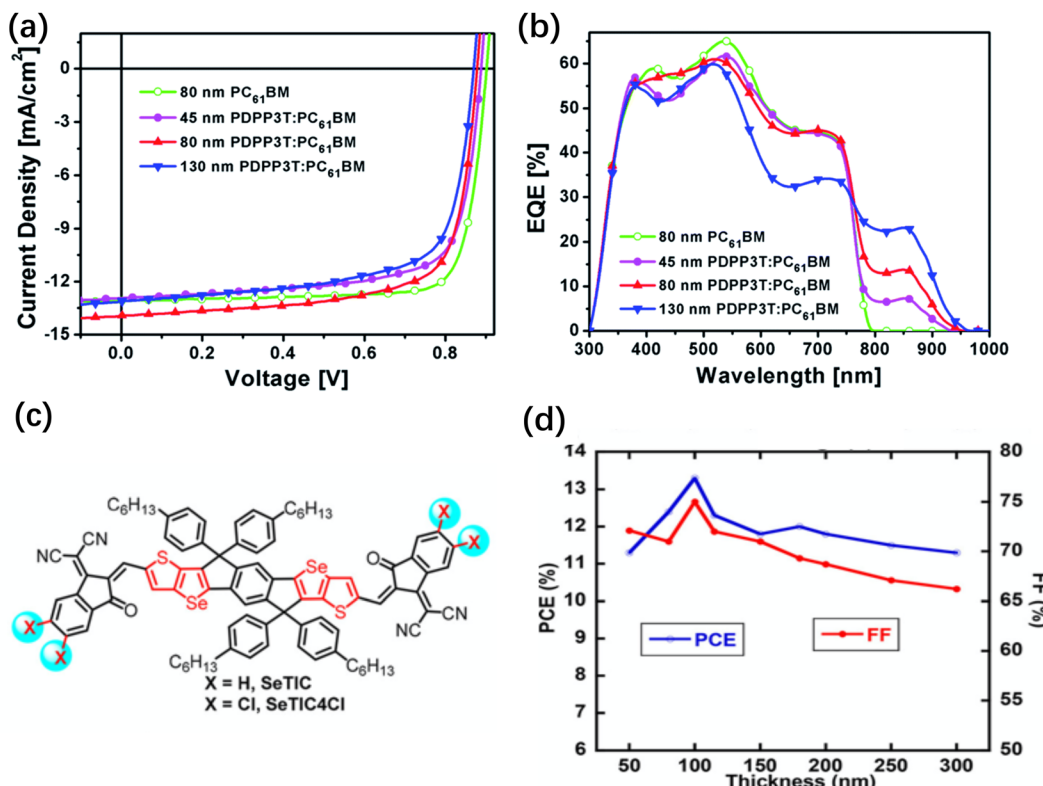


**FIG. 10.** (a) J–V curves and (b) EQE of PC<sub>61</sub>BM and PDPPP3T:PC<sub>61</sub>BM based devices. Reproduced with permission from Zuo *et al.*, *J. Mater. Chem. A* **3**, 9063 (2015). Copyright 2015 Royal Society of Chemistry. (c) Chemical structure of SeTIC4Cl. (d) PCE and FF of PM6/SeTIC4Cl BHJ OSCs showing thickness insensitivity. Reproduced with permission from Wang *et al.*, *ACS Energy Lett.* **3**, 2967 (2018). Copyright 2018 American Chemical Society.

performance over 16% in many OSCs.<sup>68,82,97,98</sup> More detailed information regarding Y6 derivatives can be found in a recent review article.<sup>2</sup> The introduction of new polymer donor D18 promoted the efficiency of Y6 based OSCs to a record value of 18.2% as well as a high photocurrent of 27.7 mA/cm<sup>2</sup>.<sup>5</sup> Until now, the IPOSOS with a Y6 based ternary BHJ layer possess the highest performance (20.6%) among all publications in this field.<sup>51</sup> These encouraging results demonstrate the feasibility to achieve high efficiency IPOSOS with Y6 derivative based BHJ layers.

c. Other high efficiency OSCs. The molecular stacking and aggregation of organic semiconductors have a significant influence on their optoelectronic properties, and ultimately impact the photovoltaic efficiency.<sup>26</sup> The complex chemical structure of non-fullerene acceptors cast versatile aggregation states in OSCs and consequently vastly different performance.<sup>108</sup> For example, COI8DFIC is a narrow bandgap acceptor with strong crystallization ability and has demonstrated versatile molecular packing forms, including flat-on and edge-on lamellae and H- and J-type aggregates.<sup>23</sup> The H-aggregates can blue shift the absorption spectrum, while the J-aggregates will red shift the absorption spectrum; however, flat-on and edge-on lamellae strengthen their absorption in the middle region. The absorption and charge mobility in COI8DFIC binary or ternary BHJs can therefore be tailored via solution casting and material blending strategy, to meet further requirements in IPOSOS.<sup>109</sup> For example, Wang *et al.* extended the

EQE response to 1050 nm with a J<sub>SC</sub> of 26.2 mA/cm<sup>2</sup> by hot-substrate casting of PTB7-Th:COI8DFIC to encourage the coexistence of H- and J-aggregation in the BHJ film, which is one of the broadest EQEs in OSCs.<sup>23</sup> IEICO-4F has been introduced into the perovskite bulk to provide extended NIR photoresponse with a high PCE of 21.6% in PSCs, and the IEICO based IPOSOS have been investigated in some works.<sup>16,46,47,59</sup> The broad absorption spectrum (over 1000 nm) and weak thickness-dependent property (maintaining 70% PCE in thick BHJ OSCs) of the IEICO-4F based BHJ would provide more photocurrent for high-performance IPOSOS.<sup>20,59,104,105,110</sup> F8IC is also a promising material for fabricating high efficiency IPOSOS. The J<sub>SC</sub> of PTB7-Th:F8IC BHJ layer based IPOSOS has reached 28.2 mA/cm<sup>2</sup> due to the wide NIR absorption over 1000 nm, although the corresponding PCE was lower than the PTB7-Th based PSCs.<sup>39</sup> Further tailoring of the BHJ layer, such as PM6:IT-4F:F8IC, with high exciton separation and charge transport efficiency may be able to improve the performance of IPOSOS.<sup>107</sup>

### C. Perovskite layer

The wide bandgap perovskites in IPOSOS usually employ MAPbI<sub>3-x</sub>Cl<sub>x</sub>, MAPbI<sub>3</sub>, and (FAPbI<sub>3</sub>)<sub>0.85</sub>(MAPbBr<sub>3</sub>)<sub>0.15</sub> (see Table I), which can sufficiently absorb light below 800 nm and quickly transport charge carriers to corresponding electrodes benefiting from their high absorption coefficient and charge carrier mobility.<sup>37,40,48</sup> Other

perovskites, e.g., mixed anion perovskite  $\text{Cs}_{0.12}\text{MA}_{0.05}\text{FA}_{0.83}\text{PbI}_{1.8}\text{Br}_{1.2}$  and inorganic  $\text{CsPbI}_2\text{Br}$  based PSCs can obtain high  $V_{OC}$  over 1.25 and 1.4 V, respectively (see summary in Table IV), with comparable performance compared to  $\text{MAPbI}_{3-x}\text{Cl}_x$  perovskite, which are conducive to acquire higher performance in IPOS Cs due to the high  $V_{OC}$ .<sup>111–113</sup> While  $\text{CsPbBr}_3$  based PSC can achieve an even higher  $V_{OC}$  of 1.59 V, the relatively low  $J_{SC}$  of this PSC hinders the use of  $\text{CsPbBr}_3$  as an promising perovskite layer in IPOS Cs.<sup>114</sup>

Tan and co-workers first employed non-fullerene narrow bandgap acceptor IEICO to extend the NIR photoresponse in  $\text{MAPbI}_3$  based IPOS Cs. The PBDTTT-E-T:IEICO BHJ layer extended the photoresponse of IPOS Cs to 930 nm and elevated the EQE intensity in the NIR region to over 50%, resulting in the substantial increase in  $J_{SC}$  from 21.81 to 24.48 mA/cm<sup>2</sup> compared to Spiro-OMeTAD based PSCs. However, the FF was reduced from 74.49 to 60.97% thus the PCE was decreased from 18.06 to 14.57%.<sup>46</sup> Afterwards, they employed wider bandgap inorganic perovskite  $\text{CsPbI}_2\text{Br}$  ( $E_g = 1.85$  eV) to replace  $\text{MAPbI}_3$  ( $E_g = 1.53$  eV) in PBDTTT-E-T:IEICO based IPOS Cs. Compared to the Spiro-OMeTAD based  $\text{CsPbI}_2\text{Br}$  PSCs, the obviously increased  $J_{SC}$  (14.78 to 15.98 mA/cm<sup>2</sup>) of IPOS Cs with nearly identical  $V_{OC}$  and FF contributed to the increase in efficiency from 12.53 to 14.03%. The photoinduced transient absorption spectroscopy indicates that the  $\text{CsPbI}_2\text{Br}$  and PBDTTT-E-T:IEICO BHJ blends could generate charge carriers simultaneously, and the BHJ layer could quickly extract electrons from the  $\text{CsPbI}_2\text{Br}$  layer, which contributes to the improvement of performance.<sup>47</sup> Though the final performance of  $\text{CsPbI}_2\text{Br}$  based IPOS Cs is not high enough, the selection of perovskite with high  $V_{OC}$  will give new opportunities to increase performance.

Besides the choice of perovskite materials, the morphology within the perovskite layer, i.e., crystallinity, grain size, and film uniformity can also be tuned, which also influence charge transport and recombination to determine efficiency. Dedicated review on morphology control in PSCs can be found in the literature.<sup>1,138–140</sup>

At the BHJ/perovskite interface, the formation of a gradient heterojunction across two adjacent layers is an effective way to promote charge generation, where the exciton dissociation of organic materials can be realized in organic BHJ and perovskite layers simultaneously. The sufficient contact between organic materials and perovskite is also beneficial to provide defect passivation effects by those electron-rich units of organic materials. Liao and co-workers prepared PTB7:ITIC blends in antisolvent to drop on the fresh wet  $\text{MAPbI}_3$  film to form a graded BHJ throughout the whole photoactive layer.<sup>52</sup> The introduction of PTB7:ITIC BHJ enhanced hole and electron mobility of the perovskite layer and promoted absorption and EQE intensities in the range of 550–750 nm, leading to the remarkable increases in  $J_{SC}$  (21.3 to 24.2 mA/cm<sup>2</sup>) and PCE (16.77 to 20.00%).<sup>52</sup> This graded BHJ is also beneficial to overcome the interfacial barrier and align the energy level between the perovskite and organic BHJ layer, avoiding the possible accumulation at the perovskite/BHJ interface and leading to efficient IPOS Cs.<sup>50</sup>

## V. CONCLUSIONS AND OUTLOOK

In summary, IPOS Cs deserve further investigation although encouraging works have been reported. A fundamental understanding of interactions between NIR organic materials and perovskite and the operational mechanism of IPOS Cs will help to further enhance device efficiency. Currently, the majority of IPOS Cs can obtain high  $J_{SC}$

**TABLE IV.** Optoelectronic properties of common perovskites incorporated into PSCs. Absorption onsets are calculated by bandgap of perovskites. CBM: conduction band minimum. VBM: valence band maximum.

Perovskite	CBM (eV)	VBM (eV)	$E_g$ (eV)	Absorption onset (nm)	$J_{SC}$ (mA/cm <sup>2</sup> )	$V_{OC}$ (V)	PCE (%)	Refs.
$\text{MAPbI}_3$	-3.75	-5.30	1.55	800	-22.5	1.15	20.9	<a href="#">115</a>
$\text{MAPbI}_{3-x}\text{Cl}_x$	-4.20	-5.82	1.62	765	-23.1	1.12	20.1	<a href="#">116</a>
$\text{MAPbI}_{2.7}\text{Br}_{0.3}$	-3.70	-5.40	1.70	729	-18.3	1.07	16.1	<a href="#">117,118</a>
$\text{FA}_{0.3}\text{MA}_{0.7}\text{PbI}_3$	-3.87	-5.40	1.53	810	-24.8	1.11	21.9	<a href="#">119,120</a>
$\text{FA}_{0.85}\text{MA}_{0.15}\text{PbI}_3$	-4.05	-5.60	1.55	800	-25.4	1.05	20.6	<a href="#">121,122</a>
$(\text{FAPbI}_3)_x(\text{MAPbBr}_3)_{1-x}$	-4.36	-5.89	1.53	810	-24.9	1.16	23.6	<a href="#">123,124</a>
$(\text{FAPbI}_3)_{0.85}(\text{MAPbBr}_3)_{0.15}$	-4.11	-5.67	1.56	795	-22.5	1.21	21.5	<a href="#">44,111</a>
$(\text{FAPbI}_3)_{0.83}(\text{MAPbBr}_3)_{0.17}$	-4.21	-5.83	1.62	765	-23.4	1.12	17.6	<a href="#">125</a>
$\text{FAPbI}_3$	-4.13	-5.60	1.47	843	-24.7	1.06	20.2	<a href="#">126,127</a>
$\text{Cs}_{0.1}\text{FA}_{0.9}\text{PbI}_3$	-4.04	-5.57	1.53	810	-22.9	1.07	18.9	<a href="#">128</a>
$\text{Cs}_{0.15}\text{FA}_{0.85}\text{PbI}_{2.7}\text{Br}_{0.3}$	-3.80	-5.40	1.60	775	-23.2	1.11	20.7	<a href="#">129</a>
$\text{Cs}_{0.2}\text{FA}_{0.8}\text{PbI}_{2.55}\text{Br}_{0.75}$	...	...	1.67	743	-20.4	1.17	18.5	<a href="#">113</a>
$\text{Cs}_{0.05}\text{MA}_{0.15}\text{FA}_{0.8}\text{PbI}_{2.55}\text{Br}_{0.75}$	...	...	1.65	752	-21.2	1.22	20.8	<a href="#">113</a>
$\text{Cs}_{0.12}\text{MA}_{0.05}\text{FA}_{0.83}\text{PbI}_{1.8}\text{Br}_{1.2}$	...	...	1.74	713	-19.0	1.25	19.3	<a href="#">113</a>
$\text{CsPbI}_3$	-3.12	-4.80	1.68	738	-20.2	1.14	19.0	<a href="#">130,131</a>
$\text{CsPbI}_{2.85}\text{Br}_{0.15}$	-3.70	-5.42	1.72	721	-19.8	1.14	17.2	<a href="#">132</a>
$\text{CsPbI}_{3-x}\text{Br}_x$	-3.96	-5.71	1.75	708	-18.3	1.23	18.6	<a href="#">133</a>
$\text{CsPbI}_2\text{Br}$	-3.86	-5.77	1.91	649	-14.3	1.41	15.5	<a href="#">134</a>
$\text{CsPbIBr}_2$	-3.49	-5.53	2.04	608	-12.3	1.21	10.6	<a href="#">135,136</a>
$\text{CsPbBr}_3$	-3.30	-5.60	2.30	540	-7.5	1.59	10.1	<a href="#">114,137</a>

values, however, the low charge mobility of organic BHJs and energy level misalignment between perovskite and organic BHJ will induce severe charge recombination, consequently leading to dramatically reduced FF and ultimately the decreased device PCE. How to design and fabricate BHJ layers with high carrier mobilities is the most urgent problem to be solved. Besides, the narrow bandgap donors, designed to compensate light absorption with fullerene and non-fullerene acceptors, cannot block electrons in conventional IPOSAs due to their deep LUMO energy levels and requires further material design. Benefiting from the emergence of new organic semiconductors, IPOSAs incorporating the BHJ layer made from narrow bandgap acceptor/wide bandgap donor are the future direction of device fabrication. As morphological and energetic defects commonly exist in perovskites, defect passivation via various organic moieties of the BHJ layer should be considered and explored to enhance the stability of IPOSAs. The journey of IPOSAs fulfills opportunities and challenges. With the careful selection of photovoltaic materials and rational design of device architectures, high performance IPOSAs can certainly be realized to break the S-Q limitation.

## ACKNOWLEDGMENTS

We acknowledge funding support from the National Natural Science Foundation of China (No. 51861145101) and the Fundamental Research Funds for the Central Universities (WUT: 2019-YB-004) of China.

## DATA AVAILABILITY

The data that support the findings of this study are available within the article.

## REFERENCES

- <sup>1</sup>L. Yang, A. T. Barrows, D. G. Lidzey, and T. Wang, "Recent progress and challenges of organometal halide perovskite solar cells," *Rep. Prog. Phys.* **79**, 026501 (2016).
- <sup>2</sup>S. Li, C. Li, M. Shi, and H. Chen, "New phase for organic solar cell research: Emergence of Y-series electron acceptors and their perspectives," *ACS Energy Lett.* **5**, 1554–1567 (2020).
- <sup>3</sup>Y. Zhang, G. Wu, F. Liu, C. Ding, Z. Zou, and Q. Shen, "Photoexcited carrier dynamics in colloidal quantum dot solar cells: Insights into individual quantum dots, quantum dot solid films and devices," *Chem. Soc. Rev.* **49**, 49–84 (2020).
- <sup>4</sup>NREL, [https://www.nrel.gov/pv/assets/pdfs/best-research-cell-efficiencies.\(.-page unavailable\) \(Last accessed May 10, 2020\).](https://www.nrel.gov/pv/assets/pdfs/best-research-cell-efficiencies.(.-page unavailable) (Last accessed May 10, 2020).)
- <sup>5</sup>Q. Liu, Y. Jiang, K. Jin, J. Qin, J. Xu, W. Li, J. Xiong, J. Liu, Z. Xiao, K. Sun, S. Yang, X. Zhang, and L. Ding, "18% efficiency organic solar cells," *Sci. Bull.* **65**, 272–275 (2020).
- <sup>6</sup>W. Shockley and H. J. Queisser, "Detailed balance limit of efficiency of p-n junction solar cells," *J. Appl. Phys.* **32**, 510–519 (1961).
- <sup>7</sup>A. Polman, M. Knight, E. C. Garnett, B. Ehrler, and W. C. Sinke, "Photovoltaic materials: Present efficiencies and future challenges," *Science* **352**, aad4424 (2016).
- <sup>8</sup>B. Chen, X. Zheng, Y. Bai, N. P. Padture, and J. Huang, "Progress in tandem solar cells based on hybrid organic-inorganic perovskites," *Adv. Energy Mater.* **7**, 1602400 (2017).
- <sup>9</sup>E. Busby, J. Xia, Q. Wu, J. Z. Low, R. Song, J. R. Miller, X. Zhu, L. M. Campos, and M. Y. Sfeir, "A design strategy for intramolecular singlet fission mediated by charge-transfer states in donor–acceptor organic materials," *Nat. Mater.* **14**, 426–433 (2015).
- <sup>10</sup>M. Einzinger, T. Wu, J. F. Komppala, H. L. Smith, C. F. Perkinson, L. Nienhaus, S. Wieghold, D. N. Congreve, A. Kahn, M. G. Bawendi, and M. A. Baldo, "Sensitization of silicon by singlet exciton fission in tetracene," *Nature* **571**, 90–94 (2019).
- <sup>11</sup>Y. Hou, E. Aydin, M. De Bastiani, C. Xiao, F. H. Isikgor, D. Xue, B. Chen, H. Chen, B. Bahrami, A. H. Chowdhury, A. Johnston, S. Baek, Z. Huang, M. Wei, Y. Dong, J. Troughton, R. Jalmood, A. J. Mirabelli, T. G. Allen, E. Van Kerschaver, M. I. Saidaminov, D. Baran, Q. Qiao, K. Zhu, S. De Wolf, and E. H. Sargent, "Efficient tandem solar cells with solution-processed perovskite on textured crystalline silicon," *Science* **367**, 1135–1140 (2020).
- <sup>12</sup>S. Gharibzadeh, I. M. Hossain, P. Fassl, B. A. Nejand, T. Abzieher, M. Schultes, E. Ahlsweide, P. Jackson, M. Powalla, S. Schäfer, M. Rienäcker, T. Wietler, R. Peibst, U. Lemmer, B. S. Richards, and U. W. Paetzold, "2D/3D heterostructure for semitransparent perovskite solar cells with engineered bandgap enables efficiencies exceeding 25% in four-terminal tandems with silicon and CIGS," *Adv. Funct. Mater.* **30**, 1909919 (2020).
- <sup>13</sup>A. Karani, L. Yang, S. Bai, M. H. Futscher, H. J. Snaith, B. Ehrler, N. C. Greenham, and D. Di, "Perovskite/colloidal quantum dot tandem solar cells: Theoretical modeling and monolithic structure," *ACS Energy Lett.* **3**, 869–874 (2018).
- <sup>14</sup>P. Cheng, Y. Liu, S.-Y. Chang, T. Li, P. Sun, R. Wang, H.-W. Cheng, T. Huang, L. Meng, S. Nuryyeva, C. Zhu, K.-H. Wei, B. Sun, X. Zhan, and Y. Yang, "Efficient tandem organic photovoltaics with tunable rear sub-cells," *Joule* **3**, 432–442 (2019).
- <sup>15</sup>Y. Hu, L. Song, Y. Chen, and W. Huang, "Two-terminal perovskites tandem solar cells: Recent advances and perspectives," *Sol. RRL* **3**, 1900080 (2019).
- <sup>16</sup>C. Wang, Y. Bai, Q. Guo, C. Zhao, J. Zhang, S. Hu, T. Hayat, A. Alsaedi, and Z. Tan, "Enhancing charge transport in an organic photoactive layer via vertical component engineering for efficient perovskite/organic integrated solar cells," *Nanoscale* **11**, 4035–4043 (2019).
- <sup>17</sup>Y. Liu, Z. Hong, Q. Chen, W. Chang, H. Zhou, T.-B. Song, E. Young, Y. Yang, J. You, G. Li, and Y. Yang, "Integrated perovskite/bulk-heterojunction toward efficient solar cells," *Nano Lett.* **15**, 662–668 (2015).
- <sup>18</sup>Y. Liu and Y. Chen, "Integrated perovskite/bulk-heterojunction organic solar cells," *Adv. Mater.* **32**, 1805843 (2020).
- <sup>19</sup>J. Wang, K. Liu, L. Hong, G. Ge, C. Zhang, and J. Hou, "Selenopheno[3,2-b] thiophene-based narrow-bandgap nonfullerene acceptor enabling 13.3% efficiency for organic solar cells with thickness-insensitive feature," *ACS Energy Lett.* **3**, 2967–2976 (2018).
- <sup>20</sup>C. Yang, J. Zhang, N. Liang, H. Yao, Z. Wei, C. He, X. Yuan, and J. Hou, "Effects of energy-level offset between a donor and acceptor on the photovoltaic performance of non-fullerene organic solar cells," *J. Mater. Chem. A* **7**, 18889–18897 (2019).
- <sup>21</sup>B. Kan, H. Feng, H. Yao, M. Chang, X. Wan, C. Li, J. Hou, and Y. Chen, "A chlorinated low-bandgap small-molecule acceptor for organic solar cells with 14.1% efficiency and low energy loss," *Sci. China Chem.* **61**, 1307–1313 (2018).
- <sup>22</sup>J. J. Yuan, Y. Zhang, L. Zhou, G. Zhang, H.-L. Yip, T.-K. Lau, X. Lu, C. Zhu, H. Peng, P. A. Johnson, M. Leclerc, Y. Cao, J. Ulanski, Y. Li, and Y. Zou, "Single-junction organic solar cell with over 15% efficiency using fused-ring acceptor with electron-deficient core," *Joule* **3**, 1140–1151 (2019).
- <sup>23</sup>W. Li, M. Chen, J. Cai, E. L. K. Spooner, H. Zhang, R. S. Gurney, D. Liu, Z. Xiao, D. G. Lidzey, L. Ding, and T. Wang, "Molecular order control of nonfullerene acceptors for high-efficiency polymer solar cells," *Joule* **3**, 819–833 (2019).
- <sup>24</sup>S. Xu, Z. Zhou, W. Liu, Z. Zhang, F. Liu, H. Yan, and X. Zhu, "A twisted thieno[3,4-b] thiophene-based electron acceptor featuring a 14- $\pi$ -electron indenoindene core for high-performance organic photovoltaics," *Adv. Mater.* **29**, 1704510 (2017).
- <sup>25</sup>H. Yao, Y. Chen, Y. Qin, R. Yu, Y. Cui, B. Yang, S. Li, K. Zhang, and J. Hou, "Design and synthesis of a low bandgap small molecule acceptor for efficient polymer solar cells," *Adv. Mater.* **28**, 8283–8287 (2016).
- <sup>26</sup>R. S. Gurney, D. G. Lidzey, and T. Wang, "A review of non-fullerene polymer solar cells: From device physics to morphology control," *Rep. Prog. Phys.* **82**, 036601 (2019).
- <sup>27</sup>A. Pivrikas, N. S. Sariciftci, G. Juška, and R. Österbacka, "A review of charge transport and recombination in polymer/fullerene organic solar cells," *Prog. Photovoltaics Res. Appl.* **15**, 677–696 (2007).

- <sup>28</sup>B. Park and S. Il Seok, "Intrinsic instability of inorganic–organic hybrid halide perovskite materials," *Adv. Mater.* **31**, 1805337 (2019).
- <sup>29</sup>A. Mei, X. Li, L. Liu, Z. Ku, T. Liu, Y. Rong, M. Xu, M. Hu, J. Chen, Y. Yang, M. Gratzel, and H. Han, "A hole-conductor-free, fully printable mesoscopic perovskite solar cell with high stability," *Science* **345**, 295–298 (2014).
- <sup>30</sup>F. Cai, J. Cai, L. Yang, W. Li, R. S. Gurney, H. Yi, A. Iraqi, D. Liu, and T. Wang, "Molecular engineering of conjugated polymers for efficient hole transport and defect passivation in perovskite solar cells," *Nano Energy* **45**, 28–36 (2018).
- <sup>31</sup>J. Shi, Y. Li, Y. Li, D. Li, Y. Luo, H. Wu, and Q. Meng, "From ultrafast to ultra-slow: Charge-carrier dynamics of perovskite solar cells," *Joule* **2**, 879–901 (2018).
- <sup>32</sup>B. Chen, P. N. Rudd, S. Yang, Y. Yuan, and J. Huang, "Imperfections and their passivation in halide perovskite solar cells," *Chem. Soc. Rev.* **48**, 3842–3867 (2019).
- <sup>33</sup>Y. Wang, W. Chen, L. Wang, B. Tu, T. Chen, B. Liu, K. Yang, C. W. Koh, X. Zhang, H. Sun, G. Chen, X. Feng, H. Y. Woo, A. B. Djurišić, Z. He, and X. Guo, "Dopant-free small-molecule hole-transporting material for inverted perovskite solar cells with efficiency exceeding 21%," *Adv. Mater.* **31**, 1902781 (2019).
- <sup>34</sup>F. Liu, F. Wu, W. Ling, Z. Tu, J. Zhang, Z. Wei, L. Zhu, Q. Li, and Z. Li, "Facile-effective hole-transporting materials based on dibenz[a,c]carbazole: The key role of linkage position to photovoltaic performance of perovskite solar cells," *ACS Energy Lett.* **4**, 2514–2521 (2019).
- <sup>35</sup>T. M. Clarke and J. R. Durrant, "Charge photogeneration in organic solar cells," *Chem. Rev.* **110**, 6736–6767 (2010).
- <sup>36</sup>L. M. Herz, "Charge-carrier dynamics in organic-inorganic metal halide perovskites," *Annu. Rev. Phys. Chem.* **67**, 65–89 (2016).
- <sup>37</sup>C. Zuo and L. Ding, "Bulk heterojunctions push the photoresponse of perovskite solar cells to 970 nm," *J. Mater. Chem. A* **3**, 9063–9066 (2015).
- <sup>38</sup>S. Dong, Y. Liu, Z. Hong, E. Yao, P. Sun, L. Meng, Y. Lin, J. Huang, G. Li, and Y. Yang, "Unraveling the high open circuit voltage and high performance of integrated perovskite/organic bulk-heterojunction solar cells," *Nano Lett.* **17**, 5140–5147 (2017).
- <sup>39</sup>M. Zhang, T. Li, J. Yu, G. Lu, H. Zhou, and X. Zhan, "Integrated perovskite/organic photovoltaics with ultrahigh photocurrent and photoresponse approaching 1000 nm," *Sol. RRL* **4**, 2000140 (2020).
- <sup>40</sup>Y. Zhang, W. Yu, W. Qin, Z. Yang, D. Yang, Y. Xing, S. Liu, and C. Li, "Perovskite as an effective  $V_{oc}$  switcher for high efficiency polymer solar cells," *Nano Energy* **20**, 126–133 (2016).
- <sup>41</sup>W. Tress, M. Yavari, K. Domanski, P. Yadav, B. Niesen, J. P. Correa Baena, A. Hagfeldt, and M. Graetzel, "Interpretation and evolution of open-circuit voltage, recombination, ideality factor and subgap defect states during reversible light-soaking and irreversible degradation of perovskite solar cells," *Energy Environ. Sci.* **11**, 151–165 (2018).
- <sup>42</sup>C. M. Proctor, M. Kuik, and T.-Q. Nguyen, "Charge carrier recombination in organic solar cells," *Prog. Polym. Sci.* **38**, 1941–1960 (2013).
- <sup>43</sup>L. Ye, B. Fan, S. Zhang, S. Li, B. Yang, Y. Qin, H. Zhang, and J. Hou, "Perovskite-polymer hybrid solar cells with near-infrared external quantum efficiency over 40%," *Sci. China Mater.* **58**, 953–960 (2015).
- <sup>44</sup>M. Cheng, C. Chen, K. Aitola, F. Zhang, Y. Hua, G. Boschloo, L. Kloot, and L. Sun, "Highly efficient integrated perovskite solar cells containing a small molecule-PC<sub>70</sub>BM bulk heterojunction layer with an extended photovoltaic response up to 900 nm," *Chem. Mater.* **28**, 8631–8639 (2016).
- <sup>45</sup>K. Gao, Z. Zhu, B. Xu, S. B. Jo, Y. Kan, X. Peng, and A. K. Y. Jen, "Highly efficient porphyrin-based OPV/perovskite hybrid solar cells with extended photoresponse and high fill factor," *Adv. Mater.* **29**, 1703980 (2017).
- <sup>46</sup>Q. Guo, H. Liu, Z. Shi, F. Wang, E. Zhou, X. Bian, B. Zhang, A. Alsaedi, T. Hayat, and Z. Tan, "Efficient perovskite/organic integrated solar cells with extended photoresponse to 930 nm and enhanced near-infrared external quantum efficiency of over 50%," *Nanoscale* **10**, 3245–3253 (2018).
- <sup>47</sup>Q. Guo, Y. Bai, K. Lang, Z. Yu, T. Hayat, A. Alsaedi, E. Zhou, and Z. Tan, "Expanding the light harvesting of CsPbI<sub>2</sub>Br to near infrared by integrating with organic bulk heterojunction for efficient and stable solar cells," *ACS Appl. Mater. Interfaces* **11**, 37991–37998 (2019).
- <sup>48</sup>C. Chen, S. Wu, Y. Lu, C. Lee, K. Ho, Z. Zhu, W. Chen, and C. Chueh, "Enhanced near-infrared photoresponse of inverted perovskite solar cells through rational design of bulk-heterojunction electron-transporting layers," *Adv. Sci.* **6**, 1901714 (2019).
- <sup>49</sup>J. Kim, G. Kim, H. Back, J. Kong, I.-W. Hwang, T. K. Kim, S. Kwon, J.-H. Lee, J. Lee, K. Yu, C.-L. Lee, H. Kang, and K. Lee, "High-performance integrated perovskite and organic solar cells with enhanced fill factors and near-infrared harvesting," *Adv. Mater.* **28**, 3159–3165 (2016).
- <sup>50</sup>M. Daboczi, J. Kim, J. Lee, H. Kang, I. Hamilton, C. Lin, S. D. Dimitrov, M. A. McLachlan, K. Lee, J. R. Durrant, and J. Kim, "Towards efficient integrated perovskite/organic bulk heterojunction solar cells: Interfacial energetic requirement to reduce charge carrier recombination losses," *Adv. Funct. Mater.* **30**, 2001482 (2020).
- <sup>51</sup>W. Chen, H. Sun, Q. Hu, A. B. Djurišić, T. P. Russell, X. Guo, and Z. He, "High short-circuit current density via integrating the perovskite and ternary organic bulk heterojunction," *ACS Energy Lett.* **4**, 2535–2536 (2019).
- <sup>52</sup>K. Hu, Z.-K. Wang, L. Meng, K.-L. Wang, Y. Zhang, and L.-S. Liao, "Organic bulk-heterojunction injected perovskite films for highly efficient solar cells," *J. Mater. Chem. C* **7**, 6391–6397 (2019).
- <sup>53</sup>G. Xu, P. Bi, S. Wang, R. Xue, J. Zhang, H. Chen, W. Chen, X. Hao, Y. Li, and Y. Li, "Integrating ultrathin bulk-heterojunction organic semiconductor intermediary for high-performance low-bandgap perovskite solar cells with low energy loss," *Adv. Funct. Mater.* **28**, 1804427 (2018).
- <sup>54</sup>Q. An, F. Zhang, J. Zhang, W. Tang, Z. Deng, and B. Hu, "Versatile ternary organic solar cells: A critical review," *Energy Environ. Sci.* **9**, 281–322 (2016).
- <sup>55</sup>W. Li, M. Chen, Z. Zhang, J. Cai, H. Zhang, R. S. Gurney, D. Liu, J. Yu, W. Tang, and T. Wang, "Retarding the crystallization of a nonfullerene electron acceptor for high-performance polymer solar cells," *Adv. Funct. Mater.* **29**, 1807662 (2019).
- <sup>56</sup>D. Kearns and M. Calvin, "Photovoltaic effect and photoconductivity in laminated organic systems," *J. Chem. Phys.* **29**, 950–951 (1958).
- <sup>57</sup>G. Feng, J. Li, Y. He, W. Zheng, J. Wang, C. Li, Z. Tang, A. Osvet, N. Li, C. J. Brabec, Y. Yi, H. Yan, and W. Li, "Thermal-driven phase separation of double-cable polymers enables efficient single-component organic solar cells," *Joule* **3**, 1765–1781 (2019).
- <sup>58</sup>F. Wu, W. Gao, L. Zhu, H. Lu, and C. Yang, "Extending photoresponse to the near-infrared region for inverted perovskite solar cells by using a low-bandgap electron transporting material," *Sol. RRL* **4**, 1900565 (2020).
- <sup>59</sup>X. Zhao, C. Yao, T. Liu, J. C. Hamill, G. O. Ngongang Ndjawa, G. Cheng, N. Yao, H. Meng, and Y. Loo, "Extending the photovoltaic response of perovskite solar cells into the near-infrared with a narrow-bandgap organic semiconductor," *Adv. Mater.* **31**, 1904494 (2019).
- <sup>60</sup>L. Bian, E. Zhu, J. Tang, W. Tang, and F. Zhang, "Recent progress in the design of narrow bandgap conjugated polymers for high-efficiency organic solar cells," *Prog. Polym. Sci.* **37**, 1292–1331 (2012).
- <sup>61</sup>Y. Yan, F. Cai, L. Yang, J. Li, Y. Zhang, F. Qin, C. Xiong, Y. Zhou, D. G. Lidsey, and T. Wang, "Light-soaking-free inverted polymer solar cells with an efficiency of 10.5% by compositional and surface modifications to a low-temperature-processed TiO<sub>2</sub> electron-transport layer," *Adv. Mater.* **29**, 1604044 (2017).
- <sup>62</sup>J. Fan, Y. Ma, C. Zhang, C. Liu, W. Li, R. E. I. Schropp, and Y. Mai, "Thermodynamically self-healing 1D–3D hybrid perovskite solar cells," *Adv. Energy Mater.* **8**, 1703421 (2018).
- <sup>63</sup>K. Gao, J. Miao, L. Xiao, W. Deng, Y. Kan, T. Liang, C. Wang, F. Huang, J. Peng, Y. Cao, F. Liu, T. P. Russell, H. Wu, and X. Peng, "Multi-length-scale morphologies driven by mixed additives in porphyrin-based organic photovoltaics," *Adv. Mater.* **28**, 4727–4733 (2016).
- <sup>64</sup>K. Gao, L. Li, T. Lai, L. Xiao, Y. Huang, F. Huang, J. Peng, Y. Cao, F. Liu, T. P. Russell, R. A. J. Janssen, and X. Peng, "Deep absorbing porphyrin small molecule for high-performance organic solar cells with very low energy losses," *J. Am. Chem. Soc.* **137**, 7282–7285 (2015).
- <sup>65</sup>K. Gao, S. B. Jo, X. Shi, L. Nian, M. Zhang, Y. Kan, F. Lin, B. Kan, B. Xu, Q. Rong, L. Shui, F. Liu, X. Peng, G. Zhou, Y. Cao, and A. K. Y. Jen, "Over 12% efficiency nonfullerene all-small-molecule organic solar cells with sequentially evolved multilength scale morphologies," *Adv. Mater.* **31**, 1807842 (2019).
- <sup>66</sup>Z. He, B. Xiao, F. Liu, H. Wu, Y. Yang, S. Xiao, C. Wang, T. P. Russell, and Y. Cao, "Single-junction polymer solar cells with high efficiency and photo-voltage," *Nat. Photonics* **9**, 174–179 (2015).

- <sup>67</sup>V. Vohra, K. Kawashima, T. Kakara, T. Koganezawa, I. Osaka, K. Takimiya, and H. Murata, "Efficient inverted polymer solar cells employing favourable molecular orientation," *Nat. Photonics* **9**, 403–408 (2015).
- <sup>68</sup>Q. Liao, Q. Kang, Y. Yang, C. An, B. Xu, and J. Hou, "Tailoring and modifying an organic electron acceptor toward the cathode interlayer for highly efficient organic solar cells," *Adv. Mater.* **32**, 1906557 (2020).
- <sup>69</sup>Y. Cui, H. Yao, J. Zhang, K. Xian, T. Zhang, L. Hong, Y. Wang, Y. Xu, K. Ma, C. An, C. He, Z. Wei, F. Gao, and J. Hou, "Single-junction organic photovoltaic cells with approaching 18% efficiency," *Adv. Mater.* **32**, 1908205 (2020).
- <sup>70</sup>J. Zhao, Y. Li, G. Yang, K. Jiang, H. Lin, H. Ade, W. Ma, and H. Yan, "Efficient organic solar cells processed from hydrocarbon solvents," *Nat. Energy* **1**, 15027 (2016).
- <sup>71</sup>L. Elgar, P. Gao, P. Qin, M. Graetzel, and M. K. Nazeeruddin, "A hybrid lead iodide perovskite and lead sulfide QD heterojunction solar cell to obtain a panchromatic response," *J. Mater. Chem. A* **2**, 11586–11590 (2014).
- <sup>72</sup>J. C. Bijleveld, A. P. Zoombelt, S. G. J. Mathijssen, M. M. Wienk, M. Turbiez, D. M. de Leeuw, and R. A. J. Janssen, "Poly(diketopyrrolopyrrole-terthiophene) for ambipolar logic and photovoltaics," *J. Am. Chem. Soc.* **131**, 16616–16617 (2009).
- <sup>73</sup>W. Li, K. H. Hendriks, W. S. C. Roelofs, Y. Kim, M. M. Wienk, and R. A. J. Janssen, "Efficient small bandgap polymer solar cells with high fill factors for 300 nm thick films," *Adv. Mater.* **25**, 3182–3186 (2013).
- <sup>74</sup>L. Dou, C. Chen, K. Yoshimura, K. Ohya, W. Chang, J. Gao, Y. Liu, E. Richard, and Y. Yang, "Synthesis of 5H-dithieno[3,2-b:2',3'-d] pyran as an electron-rich building block for donor–acceptor type low-bandgap polymers," *Macromolecules* **46**, 3384–3390 (2013).
- <sup>75</sup>C.-C. Chen, L. Dou, J. Gao, W.-H. Chang, G. Li, and Y. Yang, "High-performance semi-transparent polymer solar cells possessing tandem structures," *Energy Environ. Sci.* **6**, 2714 (2013).
- <sup>76</sup>S. Dai, T. Li, W. Wang, Y. Xiao, T.-K. Lau, Z. Li, K. Liu, X. Lu, and X. Zhan, "Enhancing the performance of polymer solar cells via core engineering of NIR-absorbing electron acceptors," *Adv. Mater.* **30**, 1706571 (2018).
- <sup>77</sup>Y. Li, J.-D. Lin, X. Che, Y. Qu, F. Liu, L.-S. Liao, and S. R. Forrest, "High efficiency near-infrared and semitransparent non-fullerene acceptor organic photovoltaic cells," *J. Am. Chem. Soc.* **139**, 17114–17119 (2017).
- <sup>78</sup>T. Wang, A. J. Pearson, and D. G. Lidzey, "Correlating molecular morphology with optoelectronic function in solar cells based on low band-gap copolymer: Fullerene blends," *J. Mater. Chem. C* **1**, 7266 (2013).
- <sup>79</sup>L. Zhang and W. Ma, "Morphology optimization in ternary organic solar cells," *Chin. J. Polym. Sci.* **35**, 184–197 (2017).
- <sup>80</sup>M. Chen, Z. Zhang, W. Li, J. Cai, J. Yu, E. L. K. Spooner, R. C. Kilbride, D. Li, B. Du, R. S. Gurney, D. Liu, W. Tang, D. G. Lidzey, and T. Wang, "Regulating the morphology of fluorinated non-fullerene acceptor and polymer donor via binary solvent mixture for high efficiency polymer solar cells," *Sci. China Chem.* **62**, 1221–1229 (2019).
- <sup>81</sup>T. Xia, Y. Cai, H. Fu, and Y. Sun, "Optimal bulk-heterojunction morphology enabled by fibril network strategy for high-performance organic solar cells," *Sci. China Chem.* **62**, 662–668 (2019).
- <sup>82</sup>D. Li, X. Chen, J. Cai, W. Li, M. Chen, Y. Mao, B. Du, J. A. Smith, R. C. Kilbride, M. E. O'Kane, X. Zhang, Y. Zhuang, P. Wang, H. Wang, D. Liu, R. A. L. Jones, D. G. Lidzey, and T. Wang, "Non-fullerene acceptor fibrils enable efficient ternary organic solar cells with 16.6% efficiency," *Sci. China Chem.* (published online).
- <sup>83</sup>D. Qian, L. Ye, M. Zhang, Y. Liang, L. Li, Y. Huang, X. Guo, S. Zhang, Z. Tan, and J. Hou, "Design, application, and morphology study of a new photovoltaic polymer with strong aggregation in solution state," *Macromolecules* **45**, 9611–9612 (2012).
- <sup>84</sup>X. Zhu, B. Xia, K. Lu, H. Li, R. Zhou, J. Zhang, Y. Zhang, Z. Shuai, and Z. Wei, "Naphtho[1,2-b:5,6-b']dithiophene-based small molecules for thick-film organic solar cells with high fill factors," *Chem. Mater.* **28**, 943–950 (2016).
- <sup>85</sup>J. Cai, H. Wang, X. Zhang, W. Li, D. Li, Y. Mao, B. Du, M. Chen, Y. Zhuang, D. Liu, H.-L. Qin, Y. Zhao, J. A. Smith, R. C. Kilbride, A. J. Parnell, R. A. L. Jones, D. G. Lidzey, and T. Wang, "Fluorinated solid additives enable high efficiency non-fullerene organic solar cells," *J. Mater. Chem. A* **8**, 4230–4238 (2020).
- <sup>86</sup>W. Li, J. Cai, Y. Yan, F. Cai, S. Li, R. S. Gurney, D. Liu, J. D. McGettrick, T. M. Watson, Z. Li, A. J. Pearson, D. G. Lidzey, J. Hou, and T. Wang, "Correlating three-dimensional morphology with function in PBDB-T:IT-M non-fullerene organic solar cells," *Sol. RRL* **2**, 1800114 (2018).
- <sup>87</sup>R. S. Gurney, W. Li, Y. Yan, D. Liu, A. J. Pearson, and T. Wang, "Morphology and efficiency enhancements of PTB7-Th:ITIC nonfullerene organic solar cells processed via solvent vapor annealing," *J. Energy Chem.* **37**, 148–156 (2019).
- <sup>88</sup>H.-C. Liao, C.-C. Ho, C.-Y. Chang, M.-H. Jao, S. B. Darling, and W.-F. Su, "Additives for morphology control in high-efficiency organic solar cells," *Mater. Today* **16**, 326–336 (2013).
- <sup>89</sup>F. Zhao, C. Wang, and X. Zhan, "Morphology control in organic solar cells," *Adv. Energy Mater.* **8**, 1703147 (2018).
- <sup>90</sup>Y. Yan, X. Liu, and T. Wang, "Conjugated-polymer blends for organic photovoltaics: Rational control of vertical stratification for high performance," *Adv. Mater.* **29**, 1601674 (2017).
- <sup>91</sup>T. Wang, N. W. Scarratt, H. Yi, I. F. Coleman, Y. Zhang, R. T. Grant, J. Yao, M. W. A. Skoda, A. D. F. Dunbar, R. A. L. Jones, A. Iraqi, and D. G. Lidzey, "Vertical stratification and its impact on device performance in a polycarbazole based copolymer solar cells," *J. Mater. Chem. C* **3**, 4007–4015 (2015).
- <sup>92</sup>J. S. Kim, Y. Lee, J. H. Lee, J. H. Park, J. K. Kim, and K. Cho, "High-efficiency organic solar cells based on end-functional-group-modified poly(3-hexylthiophene)," *Adv. Mater.* **22**, 1355–1360 (2010).
- <sup>93</sup>J. Huang, J. H. Carpenter, C. Li, J. Yu, H. Ade, and A. K.-Y. Jen, "Highly efficient organic solar cells with improved vertical donor–acceptor compositional gradient via an inverted off-center spinning method," *Adv. Mater.* **28**, 967–974 (2016).
- <sup>94</sup>S. Feng, C. Zhang, Y. Liu, Z. Bi, Z. Zhang, X. Xu, W. Ma, and Z. Bo, "Fused-ring acceptors with asymmetric side chains for high-performance thick-film organic solar cells," *Adv. Mater.* **29**, 1703527 (2017).
- <sup>95</sup>F. Pan, L. Zhang, H. Jiang, D. Yuan, Y. Nian, Y. Cao, and J. Chen, "As-cast ternary polymer solar cells based on a nonfullerene acceptor and its fluorinated counterpart showing improved efficiency and good thickness tolerance," *J. Mater. Chem. A* **7**, 9798–9806 (2019).
- <sup>96</sup>X. Liu, L. Nian, K. Gao, L. Zhang, L. Qing, Z. Wang, L. Ying, Z. Xie, Y. Ma, Y. Cao, F. Liu, and J. Chen, "Low band gap conjugated polymers combining siloxane-terminated side chains and alkyl side chains: Side-chain engineering achieving a large active layer processing window for PCE > 10% in polymer solar cells," *J. Mater. Chem. A* **5**, 17619–17631 (2017).
- <sup>97</sup>T. Yan, W. Song, J. Huang, R. Peng, L. Huang, and Z. Ge, "16.67% rigid and 14.06% flexible organic solar cells enabled by ternary heterojunction strategy," *Adv. Mater.* **31**, 1902210 (2019).
- <sup>98</sup>B. Qiu, S. Chen, C. Sun, J. Yuan, X. Zhang, C. Zhu, S. Qin, L. Meng, Y. Zhang, C. Yang, Y. Zou, and Y. Li, "Understanding the effect of the third component PC<sub>71</sub>BM on nanoscale morphology and photovoltaic properties of ternary organic solar cells," *Sol. RRL* **4**, 1900540 (2020).
- <sup>99</sup>B. Wang, Y. Fu, Q. Yang, J. Wu, H. Liu, H. Tang, and Z. Xie, "High-efficiency ternary nonfullerene organic solar cells fabricated with a near infrared acceptor enhancing exciton utilization and extending absorption," *J. Mater. Chem. C* **7**, 10498–10506 (2019).
- <sup>100</sup>Y. Cui, H. Yao, J. Zhang, T. Zhang, Y. Wang, L. Hong, K. Xian, B. Xu, S. Zhang, J. Peng, Z. Wei, F. Gao, and J. Hou, "Over 16% efficiency organic photovoltaic cells enabled by a chlorinated acceptor with increased open-circuit voltages," *Nat. Commun.* **10**, 2515 (2019).
- <sup>101</sup>L. Zhan, S. Li, T. Lau, Y. Cui, X. Lu, M. Shi, C.-Z. Li, H. Li, J. Hou, and H. Chen, "Over 17% efficiency ternary organic solar cells enabled by two nonfullerene acceptors working in an alloy-like model," *Energy Environ. Sci.* **13**, 635–645 (2020).
- <sup>102</sup>K. Jiang, Q. Wei, J. Y. L. Lai, Z. Peng, H. K. Kim, J. Yuan, L. Ye, H. Ade, Y. Zou, and H. Yan, "Alkyl chain tuning of small molecule acceptors for efficient organic solar cells," *Joule* **3**, 3020–3033 (2019).
- <sup>103</sup>X. Song, N. Gasparini, L. Ye, H. Yao, J. Hou, H. Ade, and D. Baran, "Controlling blend morphology for ultrahigh current density in nonfullerene acceptor-based organic solar cells," *ACS Energy Lett.* **3**, 669–676 (2018).
- <sup>104</sup>Z. Wang, H. Jiang, X. Liu, J. Liang, L. Zhang, L. Qing, Q. Wang, W. Zhang, Y. Cao, and J. Chen, "Significantly enhanced electron transport of a nonfullerene acceptor in a blend film with a high hole mobility polymer of high molecular weight: Thick-film nonfullerene polymer solar cells showing a high fill factor," *J. Mater. Chem. A* **8**, 7765–7774 (2020).

- <sup>105</sup>Q. Wang, Z. Hu, Z. Wu, Y. Lin, L. Zhang, L. Liu, Y. Ma, Y. Cao, and J. Chen, "Introduction of siloxane-terminated side chains into semiconducting polymers to tune phase separation with nonfullerene acceptor for polymer solar cells," *ACS Appl. Mater. Interfaces* **12**, 4659–4672 (2020).
- <sup>106</sup>T. Chen, K. Peng, Y. Lin, Y. Su, K. Ma, L. Hong, C. Chang, J. Hou, and C. Hsu, "A chlorinated nonacyclic carbazole-based acceptor affords over 15% efficiency in organic solar cells," *J. Mater. Chem. A* **8**, 1131–1137 (2020).
- <sup>107</sup>J. Wan, L. Zhang, Q. He, S. Liu, B. Huang, L. Hu, W. Zhou, and Y. Chen, "High-performance pseudoplanar heterojunction ternary organic solar cells with nonfullerene alloyed acceptor," *Adv. Funct. Mater.* **30**, 1909760 (2020).
- <sup>108</sup>D. Li, X. Zhang, D. Liu, and T. Wang, "Aggregation of non-fullerene acceptors in organic solar cells," *J. Mater. Chem. A* (published online).
- <sup>109</sup>W. Li, Z. Xiao, J. A. Smith, J. Cai, D. Li, R. C. Kilbride, E. L. K. Spooner, O. S. Game, X. Meng, D. Liu, R. A. L. Jones, D. G. Lidzey, L. Ding, and T. Wang, "Enhancing the efficiency of PTB7-Th:COI8DFIC-based ternary solar cells with versatile third components," *Appl. Phys. Rev.* **6**, 041405 (2019).
- <sup>110</sup>Y. Cui, C. Yang, H. Yao, J. Zhu, Y. Wang, G. Jia, F. Gao, and J. Hou, "Efficient semitransparent organic solar cells with tunable color enabled by an ultralow-bandgap nonfullerene acceptor," *Adv. Mater.* **29**, 1703080 (2017).
- <sup>111</sup>D. Luo, W. Yang, Z. Wang, A. Sadhanala, Q. Hu, R. Su, R. Shivanna, G. F. Trindade, J. F. Watts, Z. Xu, T. Liu, K. Chen, F. Ye, P. Wu, L. Zhao, J. Wu, Y. Tu, Y. Zhang, X. Yang, W. Zhang, R. H. Friend, Q. Gong, H. J. Snaith, and R. Zhu, "Enhanced photovoltage for inverted planar heterojunction perovskite solar cells," *Science* **360**, 1442–1446 (2018).
- <sup>112</sup>J. Tian, Q. Xue, X. Tang, Y. Chen, N. Li, Z. Hu, T. Shi, X. Wang, F. Huang, C. J. Brabec, H. Yip, and Y. Cao, "Dual interfacial design for efficient CsPbI<sub>2</sub>Br perovskite solar cells with improved photostability," *Adv. Mater.* **31**, 1901152 (2019).
- <sup>113</sup>H. Tan, F. Che, M. Wei, Y. Zhao, M. I. Saidaminov, P. Todorović, D. Broberg, G. Walters, F. Tan, T. Zhuang, B. Sun, Z. Liang, H. Yuan, E. Fron, J. Kim, Z. Yang, O. Voznyy, M. Asta, and E. H. Sargent, "Dipolar cations confer defect tolerance in wide-bandgap metal halide perovskites," *Nat. Commun.* **9**, 3100 (2018).
- <sup>114</sup>J. Duan, Y. Zhao, X. Yang, Y. Wang, B. He, and Q. Tang, "Lanthanide ions doped CsPbBr<sub>3</sub> halides for HTM-free 10.14%-efficiency inorganic perovskite solar cell with an ultrahigh open-circuit voltage of 1.594 V," *Adv. Energy Mater.* **8**, 1802346 (2018).
- <sup>115</sup>F. Cai, Y. Yan, J. Yao, P. Wang, H. Wang, R. S. Gurney, D. Liu, and T. Wang, "Ionic additive engineering toward high-efficiency perovskite solar cells with reduced grain boundaries and trap density," *Adv. Funct. Mater.* **28**, 1801985 (2018).
- <sup>116</sup>S. Yue, K. Liu, R. Xu, M. Li, M. Azam, K. Ren, J. Liu, Y. Sun, Z. Wang, D. Cao, X. Yan, S. Qu, Y. Lei, and Z. Wang, "Efficacious engineering on charge extraction for realizing highly efficient perovskite solar cells," *Energy Environ. Sci.* **10**, 2570–2578 (2017).
- <sup>117</sup>H. Back, G. Kim, J. Kim, J. Kong, T. K. Kim, H. Kang, H. Kim, J. Lee, S. Lee, and K. Lee, "Achieving long-term stable perovskite solar cells via ion neutralization," *Energy Environ. Sci.* **9**, 1258–1263 (2016).
- <sup>118</sup>Y. Zhao and K. Zhu, "Efficient planar perovskite solar cells based on 1.8 eV band Gap CH<sub>3</sub>NH<sub>3</sub>PbI<sub>2</sub>Br nanosheets via thermal decomposition," *J. Am. Chem. Soc.* **136**, 12241–12244 (2014).
- <sup>119</sup>B. Ding, S.-Y. Huang, Q.-Q. Chu, Y. Li, C.-X. Li, C. Li, and G.-J. Yang, "Low-temperature SnO<sub>2</sub>-modified TiO<sub>2</sub> yields record efficiency for normal planar perovskite solar modules," *J. Mater. Chem. A* **6**, 10233–10242 (2018).
- <sup>120</sup>C. Liu, D. Zhang, Z. Li, W. Han, G. Ren, Z. Li, L. Shen, W. Guo, and W. Zheng, "Incorporating a polar molecule to passivate defects for perovskite solar cells," *Sol. RRL* **4**, 1900489 (2020).
- <sup>121</sup>S. Yuan, F. Qian, S. Yang, Y. Cai, Q. Wang, J. Sun, Z. Liu, and S. F. Liu, "NbF<sub>5</sub>: A novel  $\alpha$ -phase stabilizer for FA-based perovskite solar cells with high efficiency," *Adv. Funct. Mater.* **29**, 1807850 (2019).
- <sup>122</sup>F. Qian, S. Yuan, Y. Cai, Y. Han, H. Zhao, J. Sun, Z. Liu, and S. Liu, "Novel surface passivation for stable FA<sub>0.85</sub>MA<sub>0.15</sub>PbI<sub>3</sub> perovskite solar cells with 21.6% efficiency," *Sol. RRL* **3**, 1900072 (2019).
- <sup>123</sup>Q. Jiang, Y. Zhao, X. Zhang, X. Yang, Y. Chen, Z. Chu, Q. Ye, X. Li, Z. Yin, and J. You, "Surface passivation of perovskite film for efficient solar cells," *Nat. Photonics* **13**, 460–466 (2019).
- <sup>124</sup>Q. Jiang, L. Zhang, H. Wang, X. Yang, J. Meng, H. Liu, Z. Yin, J. Wu, X. Zhang, and J. You, "Enhanced electron extraction using SnO<sub>2</sub> for high-efficiency planar-structure HC(NH<sub>2</sub>)<sub>2</sub>PbI<sub>3</sub>-based perovskite solar cells," *Nat. Energy* **2**, 16177 (2017).
- <sup>125</sup>J. Zhang, S. Wu, T. Liu, Z. Zhu, and A. K.-Y. Jen, "Boosting photovoltaic performance for lead halide perovskites solar cells with BF<sub>4</sub><sup>-</sup> anion substitutions," *Adv. Funct. Mater.* **29**, 1808833 (2019).
- <sup>126</sup>W. S. Yang, J. H. Noh, N. J. Jeon, Y. C. Kim, S. Ryu, J. Seo, and S. I. Seok, "High-performance photovoltaic perovskite layers fabricated through intramolecular exchange," *Science* **348**, 1234–1237 (2015).
- <sup>127</sup>Y. Zhang, Z. Zhou, F. Ji, Z. Li, G. Cui, P. Gao, E. Oveisi, M. K. Nazeeruddin, and S. Pang, "Trash into treasure:  $\delta$ -FAPbI<sub>3</sub> polymorph stabilized MAPbI<sub>3</sub> perovskite with power conversion efficiency beyond 21%," *Adv. Mater.* **30**, 1707143 (2018).
- <sup>128</sup>N. Li, J. Liu, C. Li, Y. Li, J. Jia, Y. Wu, H. Yu, B. Yuan, and B. Cao, "Zwitterion-stabilizing scalable bladed  $\alpha$ -phase Cs<sub>0.1</sub>FA<sub>0.9</sub>PbI<sub>3</sub> films for efficient inverted planar perovskite solar cells," *ACS Sustainable Chem. Eng.* **8**, 7020–7030 (2020).
- <sup>129</sup>Y. Chen, Z. Yang, X. Jia, Y. Wu, N. Yuan, J. Ding, W.-H. Zhang, and S. Liu, "Thermally stable methylammonium-free inverted perovskite solar cells with Zn<sup>2+</sup> doped CuGaO<sub>2</sub> as efficient mesoporous hole-transporting layer," *Nano Energy* **61**, 148–157 (2019).
- <sup>130</sup>Y. Wang, M. I. Dar, L. K. Ono, T. Zhang, M. Kan, Y. Li, L. Zhang, X. Wang, Y. Yang, X. Gao, Y. Qi, M. Grätzel, and Y. Zhao, "Thermodynamically stabilized  $\beta$ -CsPbI<sub>3</sub>-based perovskite solar cells with efficiencies >18%," *Science* **365**, 591–595 (2019).
- <sup>131</sup>Y. Wang, X. Liu, T. Zhang, X. Wang, M. Kan, J. Shi, and Y. Zhao, "The role of dimethylammonium iodide in CsPbI<sub>3</sub> perovskite fabrication: Additive or dopant?," *Angew. Chem., Int. Ed.* **58**, 16691–16696 (2019).
- <sup>132</sup>H. Wang, H. Bian, Z. Jin, H. Zhang, L. Liang, J. Wen, Q. Wang, L. Ding, and S. F. Liu, "Cesium lead mixed-halide perovskites for low-energy loss solar cells with efficiency beyond 17%," *Chem. Mater.* **31**, 6231–6238 (2019).
- <sup>133</sup>Q. Ye, Y. Zhao, S. Mu, F. Ma, F. Gao, Z. Chu, Z. Yin, P. Gao, X. Zhang, and J. You, "Cesium lead inorganic solar cell with efficiency beyond 18% via reduced charge recombination," *Adv. Mater.* **31**, 1905143 (2019).
- <sup>134</sup>Z. Guo, A. K. Jena, I. Takei, G. M. Kim, M. A. Kamarudin, Y. Sanehira, A. Ishii, Y. Numata, S. Hayase, and T. Miyasaka, " $V_{oc}$  over 1.4 V for amorphous tin oxide-based dopant-free CsPbI<sub>2</sub>Br perovskite solar cells," *J. Am. Chem. Soc.* **142**, 9725–9734 (2020).
- <sup>135</sup>Y. Wang, K. Wang, W. S. Subhani, C. Zhang, X. Jiang, S. Wang, H. Bao, L. Liu, L. Wan, and S. Liu, "Extrinsic ion distribution induced field effect in CsPbIBr<sub>2</sub> perovskite solar cells," *Small* **16**, 1907283 (2020).
- <sup>136</sup>W. Zhu, Z. Zhang, W. Chai, D. Chen, H. Xi, J. Chang, J. Zhang, C. Zhang, and Y. Hao, "Benign pinholes in CsPbIBr<sub>2</sub> absorber film enable efficient carbon-based, all-inorganic perovskite solar cells," *ACS Appl. Energy Mater.* **2**, 5254–5262 (2019).
- <sup>137</sup>J. Duan, Y. Zhao, B. He, and Q. Tang, "High-purity inorganic perovskite films for solar cells with 9.72% efficiency," *Angew. Chem. Int. Ed.* **57**, 3787–3791 (2018).
- <sup>138</sup>Q. Wei, H. Bi, S. Yan, and S. Wang, "Morphology and interface engineering for organic metal halide perovskite-based photovoltaic cells," *Adv. Mater. Interfaces* **5**, 1800248 (2018).
- <sup>139</sup>J. Zhong, W. Wu, J. Liao, W. Feng, Y. Jiang, L. Wang, and D. Kuang, "The rise of textured perovskite morphology: Revolutionizing the pathway toward high-performance optoelectronic devices," *Adv. Energy Mater.* **10**, 1902256 (2020).
- <sup>140</sup>Y. Li, L. Ji, R. Liu, C. Zhang, C. H. Mak, X. Zou, H.-H. Shen, S.-Y. Leu, and H.-Y. Hsu, "A review on morphology engineering for highly efficient and stable hybrid perovskite solar cells," *J. Mater. Chem. A* **6**, 12842–12875 (2018).